

1 Charged hadron, $\pi^{+(-)}$, $K^{+(-)}$, p , and \bar{p} spectra and
2 $R_{CP}(p_T, \sqrt{s_{NN}})$ in the RHIC Beam Energy Scan
3 measured in STAR

4 Analysis note
Target Journal: PRL

James D. Brandenburg, Helen Caines, Daniel Cebra, Frank Geurts,
Stephen Horvat, Grazyna Odyniec and Evan Sangaline

5 October 18, 2016

6 **Abstract**

7 In 2010, RHIC began the Beam Energy Scan (BES) program to scan the QCD phase
8 diagram in search of a conjectured critical point and study some of the QGP signatures
9 as a function of beam energies. In 2010 and 2011 RHIC produced Au+Au collisions at
10 $\sqrt{s_{NN}} = 7.7, 11.5, 19.6, 27$, and 39 GeV. In 2014, RHIC concluded the first phase of
11 the BES program by colliding Au+Au at $\sqrt{s_{NN}} = 14.5$ GeV. In this contribution, we
12 report STAR measurements of the spectra and the nuclear modification factor R_{CP} for
13 identified $\pi^{+(-)}$, $K^{+(-)}$, and p (\bar{p}) for Au+Au collisions at this center-of-mass energy.
14 Data from multiple PID detectors are simultaneously used to extract exclusive particle
15 yields out to a p_T of 3.5 GeV/c. The measurements will be discussed in the context of
16 previously presented BES measurements.

17	Contents	
18	1 Introduction	3
19	1.1 Physics Motivation	3
20	2 Data selection	8
21	3 Event and Track Selection	9
22	3.1 Bad Run Rejection	9
23	3.2 Event Selection	10
24	3.3 Centrality Determination	13
25	3.4 Track Selection	13
26	4 Corrections	19
27	4.1 Feiddown, Knockout, and Photo-Production	19
28	4.2 Tracking Efficiency	19
29	4.3 Identified Spectra Fits for Charged Hadron Analysis	21
30	4.4 Momentum Resolution and Energy Loss	24
31	4.5 Combined Correction for Charged Hadron Analysis	26
32	5 Analysis Details : Identified Particle Spectra	31
33	5.1 Particle Identification	31
34	5.1.1 Measurement Recentering	31
35	5.1.2 Simultaneous Gaussian fit	32
36	5.2 Efficiency Corrections	39
37	5.2.1 TPC Track Reconstruction Efficiency and Acceptance	39
38	5.2.2 TOF Track Matching Efficiency	39
39	5.3 Energy Loss Corrections	48
40	5.4 Feed Down Corrections	51
41	6 Summary	58
42	A	
43	Bad Run Numbers	62

1 Introduction

1.1 Physics Motivation

Evidence has been presented that high-energy heavy-ion collisions form a dense, nearly perfect, strongly-interacting, deconfined partonic liquid called a quark gluon plasma (QGP) [1, 2, 3, 4]. This state of matter is thought to have dominated the universe prior to the hadron epoch [5]. Quantifying the properties of QGP is necessary for describing the QCD phase diagram [6]. Just as the universe followed a particular trajectory through the QCD phase diagram, so do high-energy nuclear collisions. The particular path for each collision depends on collision energy. High collision energies have low initial baryochemical potentials (μ_B) that are expected to remain low throughout the medium's evolution. This means that the trajectory passes through the region where a smooth crossover is theoretically predicted [7, 8]. Lower collision energies have been shown to produce higher μ_B [9]. A first order phase transition is predicted at sufficiently high μ_B [10, 11] which would mean the existence of a critical end point. A beam energy scan (BES) at the Relativistic Heavy-Ion Collider (RHIC) was proposed to further explore the QCD phase diagram, including a search for the critical point, and to demonstrate that signatures for QGP formation turn off at sufficiently low collision energies [12]. Hadronic suppression is a signature of QGP formation that will be examined here.

High- p_T partons produced early in the collision and moving such that they will pass through an area of QGP, would be expected to lose energy through partonic energy loss [13, 14]. Partonic energy loss has contributions from collisional and radiative energy loss with strong force analogs to the processes described in chapters 13 and 14 respectively of Jackson's iconic text [15]. This would be expected to lead to a depletion, or suppression, of high- p_T hadrons in the final state. One method of observing this suppression is with the nuclear modification factor,

$$R_{CP} = \frac{\langle N_{coll} \rangle_{\text{Peripheral}}}{\langle N_{coll} \rangle_{\text{Central}}} \frac{(\frac{d^2 N}{dp_T d\eta})_{\text{Central}}}{(\frac{d^2 N}{dp_T d\eta})_{\text{Peripheral}}}. \quad (1)$$

Here, N_{coll} is the average number of binary collisions within a centrality bin and can be estimated using a Glauber Monte Carlo [16]. Charged hadrons are measured in pseudorapidity, $d\eta$, and identified particles in rapidity, dy . If a heavy-ion collision were just a collection of N_{coll} independent $p+p$ -like collisions then R_{CP} would be unity for the entire p_T range. This observable compares the number of particles measured in small impact parameter (central) collisions where the mean pathlength through any produced medium would be longer, with large impact parameter (peripheral) collisions where the shorter in-medium pathlengths should result in less energy loss. High- p_T suppression would be expected to vanish at low collision energies where the energy density becomes too low to produce a sufficiently large and long-lived QGP. Another effect that may lead toward suppression at the lower collision energies is the EMC effect, a suppression of per nucleon cross sections in heavier nuclei relative to lighter nuclei for Bjorken $x > 0.3$ first measured with deep inelastic scattering by the European Muon Collaboration (EMC) [17]. While their measurement was for an impact

parameter averaged nuclear modification of the parton distribution function (nPDF), what we are interested in here is the impact parameter dependence of this effect [18]. Experimentally quantifying the cold nuclear matter (CNM) effects that affect these measurements would require reference data for the BES, $p(d) + Au$ and $p + p$.

High- p_T suppression was observed at top Relativistic Heavy Ion Collider (RHIC) energies soon after RHIC began running [1, 2, 3, 4] and later, at even higher energies, by experiments at the Large Hadron Collider (LHC) [19, 20].

Concealing the turn-off of partonic energy loss, a physical process that can lead to the measurement of suppression, are a series of effects that lead to enhancement. One such effect is the Cronin Effect; a CNM effect first observed in asymmetric collisions between heavy and light nuclei where an enhancement of high- p_T particles was measured rather than suppression [21, 22, 23]. It has been demonstrated that the enhancement from the Cronin Effect grows larger as the impact parameter is reduced [24, 25]. The physical processes that lead to the Cronin Effect, as well as other processes in heavy-ion collisions such as radial flow and particle coalescence [26], would be expected to compete with jet-quenching. This means that measuring a nuclear modification factor to be greater than unity does not lead us to conclude that a QGP is not formed. Disentangling these competing effects may be accomplished with complementary measurements, such as event plane dependent nuclear modification factors [27], or through other methods like the one developed in this letter.

R_{CP} takes the ratio of N_{coll} -scaled spectra from two different centralities. A more differential option for looking for jet-quenching is to look at how the N_{coll} -scaled spectra trends with centrality for a high- p_T bin,

$$Y(\langle N_{part} \rangle) = \frac{1}{\langle N_{coll} \rangle} \frac{d^2 N}{dp_T d\eta}(\langle N_{part} \rangle). \quad (2)$$

This is equivalent to taking the numerator from R_{CP} and plotting it versus centrality so that the peripheral bin contents are in the first bin at low N_{part} and the central bin's contents are in the last point at high N_{part} . Examining the full evolution with centrality allows for the disentanglement of whether the processes leading to enhancement increase faster or slower than the processes leading toward suppression as a function of centrality. While both jet-quenching and enhancement effects increase in strength with increasing N_{part} , if effects leading toward suppression increase faster then $Y(N_{part})$ decreases.

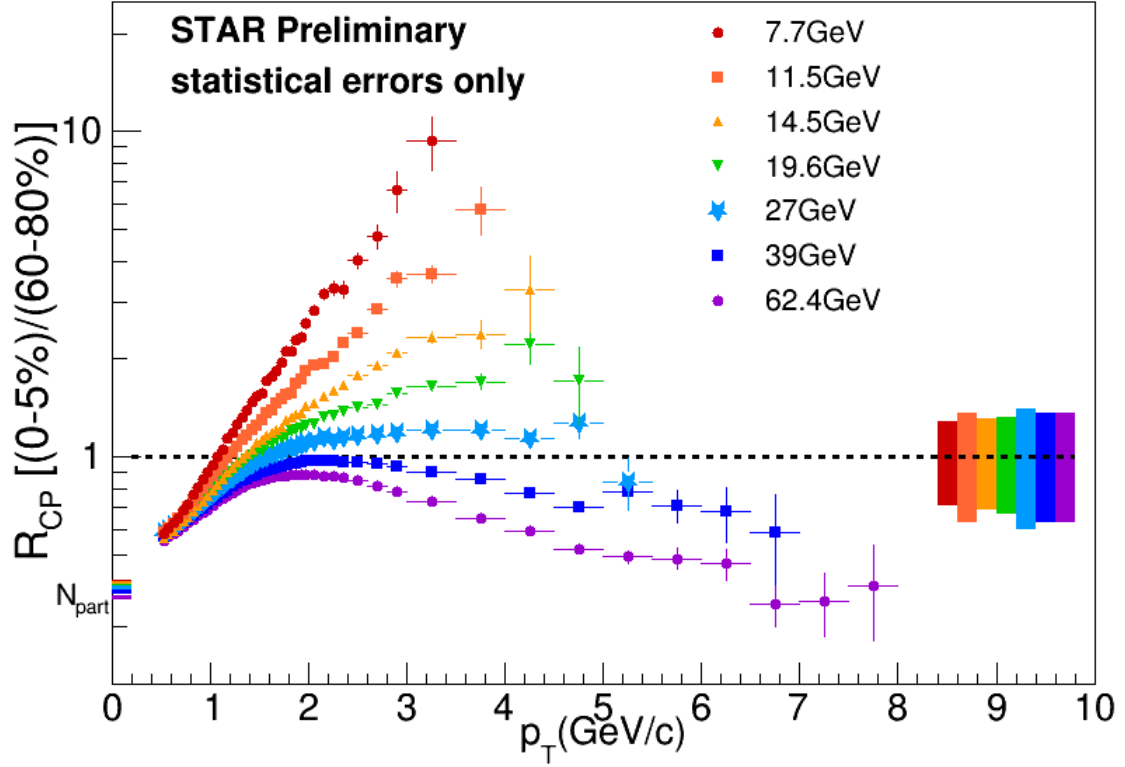


Figure 1: Charged hadron R_{CP} for RHIC BES energies. The error bands at unity on the right side of the plot correspond to the p_T independent uncertainty in N_{bin} scaling with the color in the band corresponding to the color of the data points for that energy. The vertical error bars correspond to statistical errors **and point-to-point systematics will be included.**

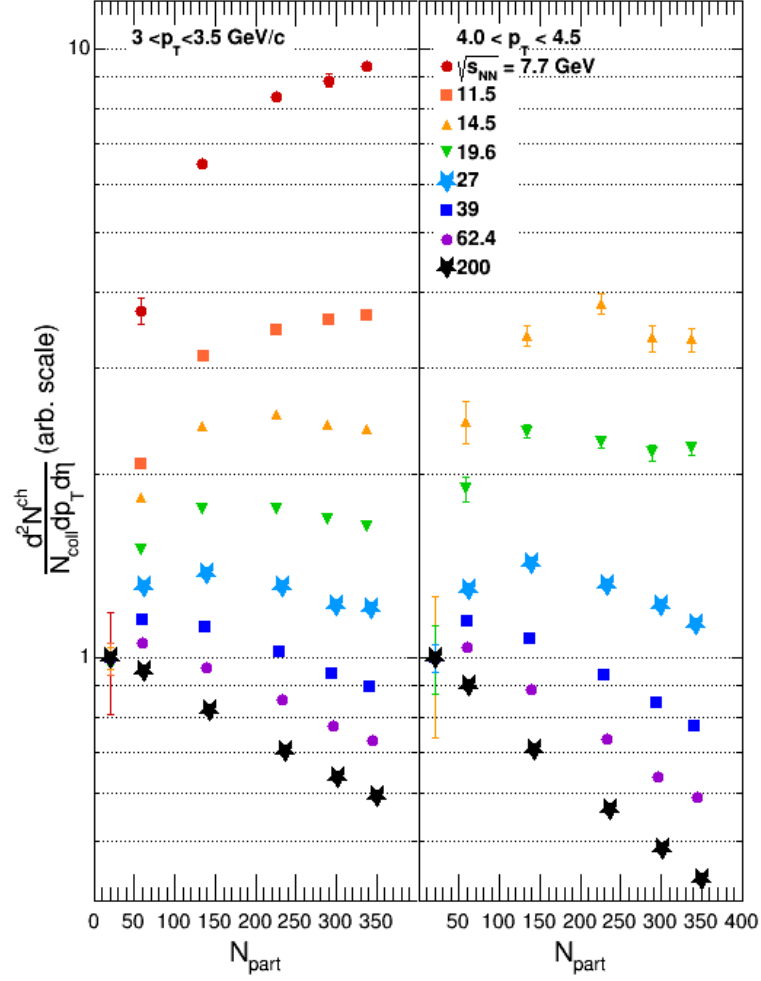


Figure 2: Charged hadron, $S(\langle N_{\text{part}} \rangle)$ for two ranges of p_T . Statistical error bars are included, mostly smaller than point size, as well as shaded boxes to indicate systematic uncertainties.

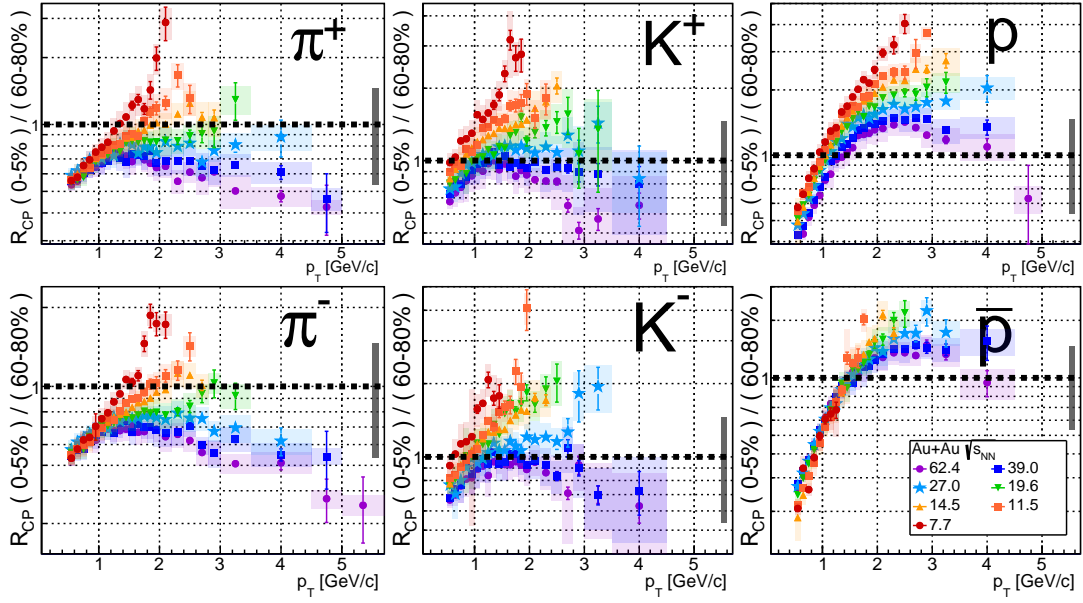


Figure 3: Identified particle R_{CP} for RHIC BES energies. The gray error band corresponds to the p_T independent uncertainty in N_{coll} scaling, while the colored shaded boxes describe the point-to-point systematic uncertainties.

Energy (GeV)	Year	Trigger IDs	Events (10^6)
7.7	2010	290001, 290004	4
11.5	2010	310004, 310014	12
14.5	2014	440005, 440015	20
19.6	2011	340001, 340011, 340021	36
27	2011	360001	70
39	2010	280001	130
62.4	2010	270011, 270021	67
200	2010	260001, 260011, 260021, 260031	350

Table 1: Data used in these analyses.

2 Data selection

The data for this analysis were collected in the 2010, 2011, and 2014 RHIC runs by the STAR detector [28], as shown in Table 1. STAR is a large acceptance detector whose tracking and particle identification for this analysis were provided by its Time Projection Chamber (TPC) [29] and Time-of-Flight (TOF) [30] detectors. These detectors lie within a 0.5 T magnetic field to bend the paths of the charged particles traversing it for momentum determination and charge discrimination.

3 Event and Track Selection

3.1 Bad Run Rejection

One important type of QA is looking for time dependent variation in quantities that would be expected to remain constant. Run averaged pseudorapidity, phi, or vertex position might be expected to change from run to run as the RHIC beam is steered and as sectors of the TPC have anode voltages altered, but average transverse momentum, charge, and other physics quantities would be expected to remain constant. A mapping between the run indices used in these plots and the actual run numbers can be found in the code StRcpMaker.cxx. This sort of bad run identification was also used by StRefMultCorr, and the bad runs identified in that class were also rejected in these analyses.

For this analysis bad runs were rejected using number of events, the average BBC coincidence rate, average primary track p_T and average reference multiplicity(refmult) observables. In addition to the bad-runs found by cutting on these run-averaged values, it was also found that all data in the Run14 AuAu14.5 dataset before day 53 is unusable due to an issue in the vertex reconstructions caused by bad BEMC input. This analysis uses data after and including day 53 with the runs in Table 10 removed. The cuts shown in Table 2 for average primary track p_T , average refmult, and average BBC coincidence rate are with respect to the average of these values for all runs in the dataset.

Table 2: Rejection of Bad Runs

Quantity	Cut
Primary Track p_T	3.2σ
RefMult	4.0σ
BBC Coincidence Rate	5.0σ
Number of Events	< 500

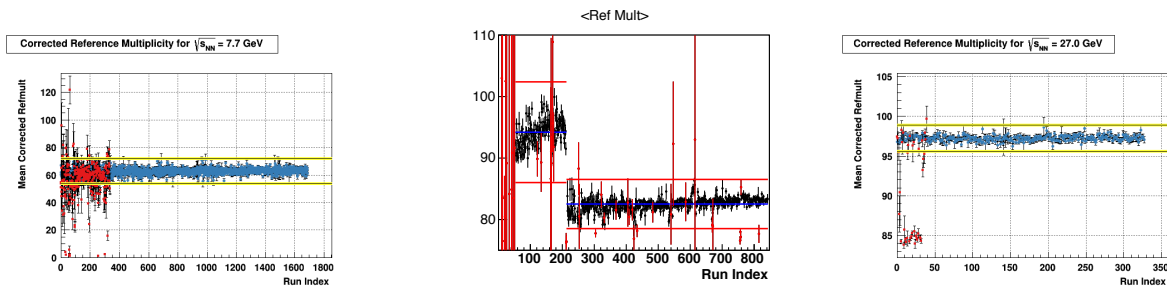


Figure 4: Run-averaged refmult vs. run-index with runs found as bad highlighted in red. Shown for $\sqrt{s_{NN}} = 7.7$ (left), 14.5 (center), and 27.0 (right) GeV.

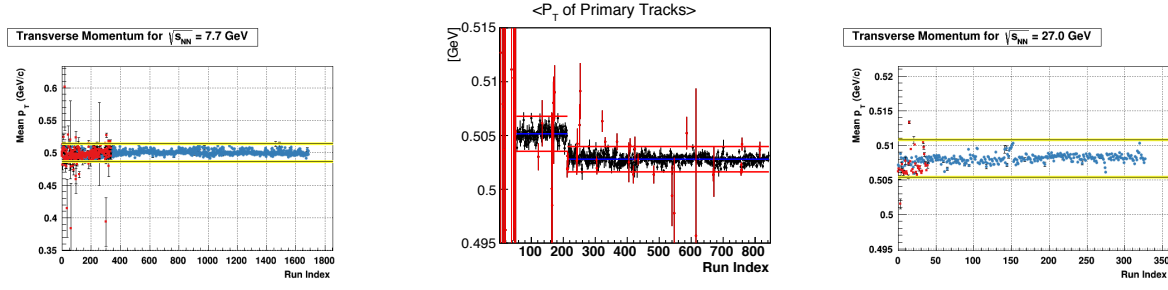


Figure 5: Run-averaged p_T of primary tracks vs. run-index with runs found as bad highlighted in red. Shown for $\sqrt{s_{NN}} = 7.7$ (left), 14.5 (center), and 27.0 (right) GeV.

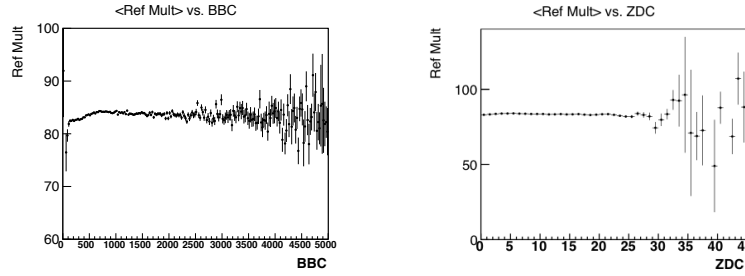


Figure 6: Mean refmult vs. BBC (left) and ZDC (right) coincidence rates for Au+Au collisions at $\sqrt{s_{NN}} = 14.5$ GeV.

3.2 Event Selection

The reconstructed vertex is required to be within 30 cm of the detector center along the beam direction. The radial vertex position is required to be within 1 cm of the mean. The 7.7 GeV dataset has a shift in this mean position part way through the run, but this is the only energy where the mean shifts significantly in a time dependent way. For the 200 GeV dataset, the reconstructed z vertex is required to be within 3 cm of the z vertex given by the VPD. Due to worsening VPD resolution, a similar requirement is not applied to the lower energies. Events are also required to have at least two TOF-matched tracks to eliminate out-of-time events.

Events used in this analysis were collected with the minimum bias triggers from the good runs.

Only events in the center of the TPC ($-30 \text{ [cm]} < z \text{ vertex} < 30 \text{ [cm]}$) are accepted. In this region of the detector the acceptance and efficiency corrections are fairly constant. A radial vertex cut of vertex R $< 1.0 \text{ [cm]}$ is applied to reduce the number of events due to beam pipe interactions. Finally, a cut on the number of TOF-matched tracks is applied. This cut rejects events in the full refmult range with low quality tracks. It is also in place to reject events without a valid TOF start time, since the TOF used “startless” mode for this dataset.

Table 3: Event Level Cuts

Quantity	Cut
Z Vertex (vZ)	$-30 \text{ [cm]} \leq \text{vZ} \leq 30 \text{ [cm]}$
R Vertex (vR)	$\text{vR} < 1.0 \text{ [cm]}$ from (0, -0.89)
# Tof-Matched Tracks (nTofMatch)	$\text{nTofMatch} \geq 3$

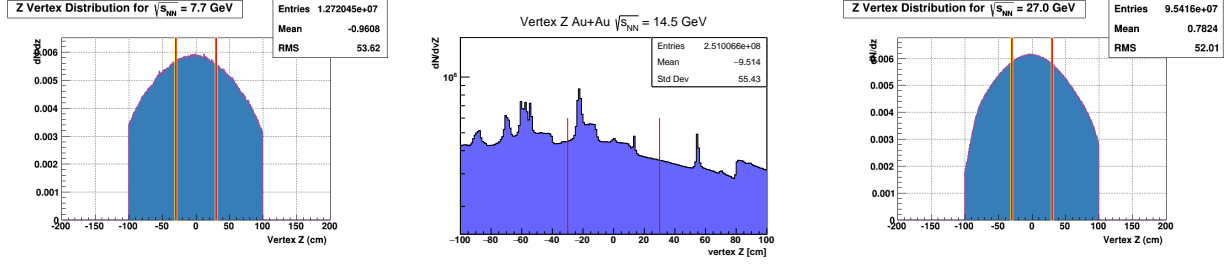


Figure 7: Z Vertex distribution with the cuts show in red vertical lines. Shown for $\sqrt{s_{NN}} = 7.7$ (left), 14.5 (center), and 27.0 (right) GeV.

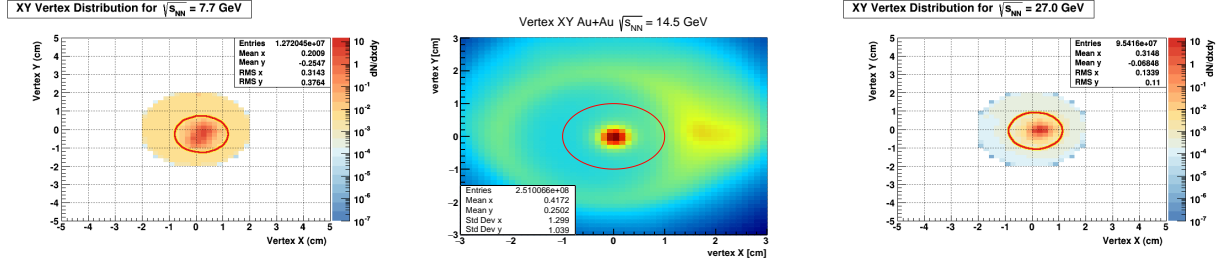


Figure 8: Y vertex vs. X vertex position with the cuts show as the red circle. Shown for $\sqrt{s_{NN}} = 7.7$ (left), 14.5 (center), and 27.0 (right) GeV.

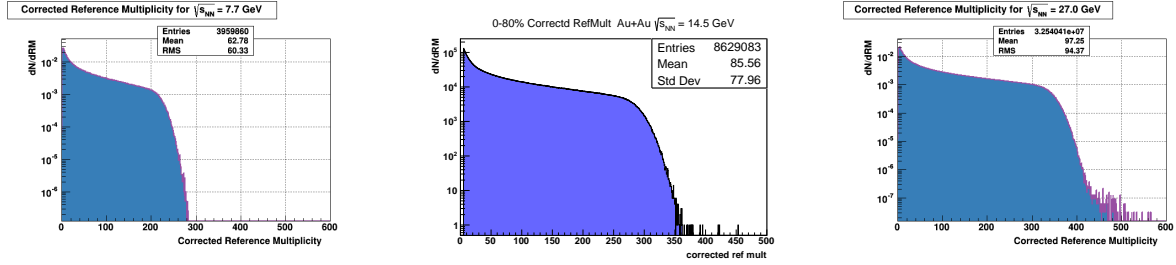


Figure 9: Corrected refmult. Shown for $\sqrt{s_{NN}} = 7.7$ (left), 14.5 (center), and 27.0 (right) GeV.

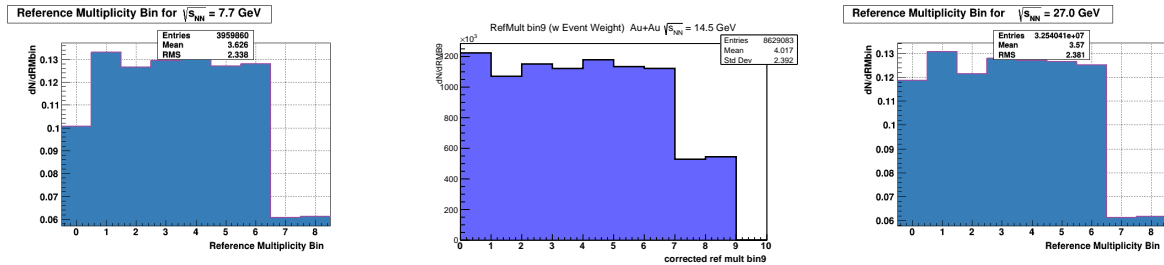


Figure 10: Refmult bins. Shown for $\sqrt{s_{NN}} = 7.7$ (left), 14.5 (center), and 27.0 (right) GeV.

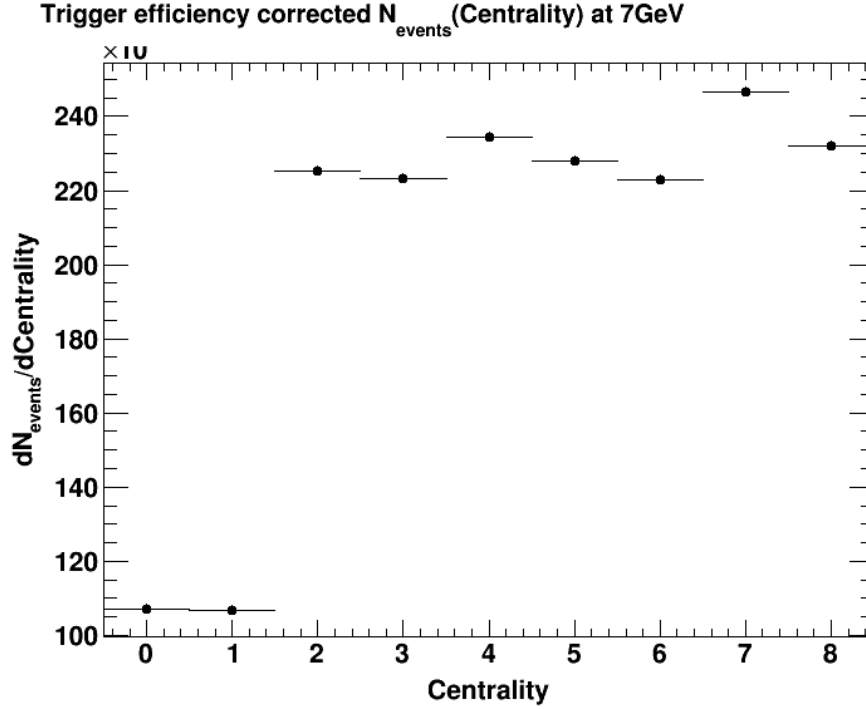


Figure 11: Number of events in each centrality bin with a trigger efficiency correction from StRefMultCorr.

3.3 Centrality Determination

StRefMultCorr is used for centrality determination, correcting for the vertex position dependence of the multiplicity. The function `GetWeight()` of StRefMultCorr is used to correct for trigger efficiency. Without this correction, the peripheral spectra would be biased toward the central side of their respective centrality bins. After this correction, the distribution of the number of events in each peripheral centrality bin is seen to be much more even (Fig. 11) than if the correction is not applied (Fig. 12).

3.4 Track Selection

For this analysis several track quality cuts are applied as shown in Table 4.

Tracks are required to have at least 16 fit points, $N_{\text{fit}}/N_{\text{poss}} > 0.52$, 11 dEdx points, and to have a dca of 1 cm or less. Tracks are accepted within a pseudo-rapidity window of -0.5 to 0.5. The transverse momentum is not allowed to change by too large of an amount when including the vertex as a fit point by requiring the primary transverse momentum to be greater than 7/10 times and less than 10/7 times the global transverse momentum.

The cuts listed in Table 4 on the number of Fit Points and ratio of Fit Points over Possible Fit Points are standard cuts used to reject low quality TPC tracks. The global DCA cut is used to select tracks that originate from the primary interaction vertex. The cut

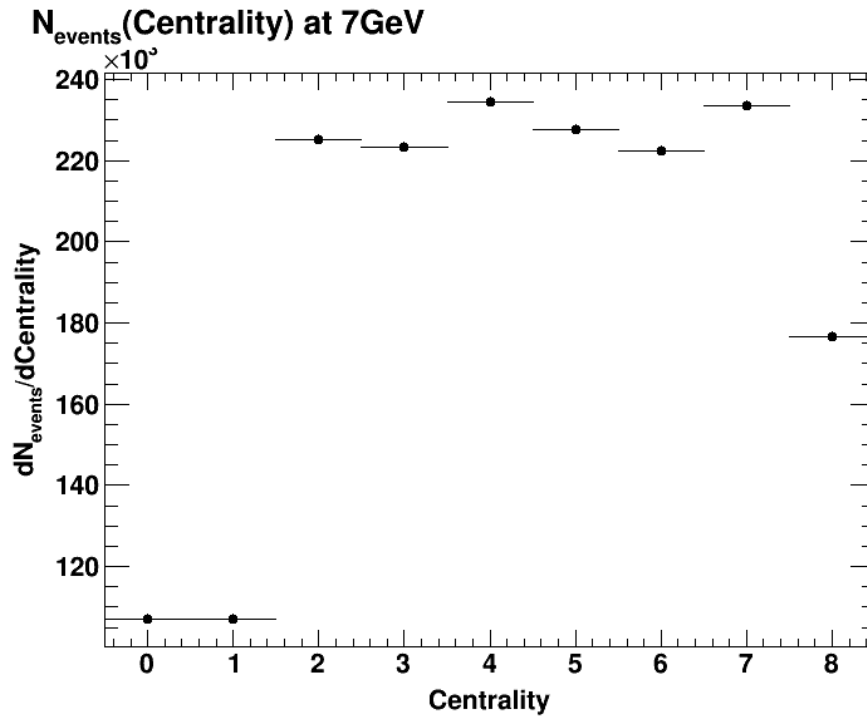


Figure 12: Number of events in each centrality bin without a trigger efficiency correction from StRefMultCorr.

Table 4: Analysis Track Level Cuts

Quantity	Cut
Number of Fit Points	$16 \leq \text{Fit Points}$
Global Track Distance to Closest Approach	$\text{DCA} \leq 1 \text{ [cm]}$
Ratio of Fit Points / Possible Fit Points	$0.52 < \text{Fit Points} / \text{Possible Fit Points}$
dE/dx Fit Points	$11 \leq \text{dE/dx Fit Points}$
Primary Track Transverse Momentum	$0.2 \text{ GeV}/c \leq p_T$
Global pT Over Primary pT	$7/10 < \text{Global pT} / \text{Primary pT} < 10/7$
Flag	$0 < \text{flag} < 1000$
Rapidity	$-0.25 < y < 0.25$

Table 5: Analysis Track Level Cuts for PID analysis only

Quantity	Cut
ToF Matched Track	ToF Match-Flag ≥ 1
ToF Y-Local Position	$-1.6 \text{ [cm]} < Y\text{-Local} < 1.6 \text{ [cm]}$
ToF Z-Local Position	$-2.8 \text{ [cm]} < Z\text{-Local} < 2.8 \text{ [cm]}$
ToF β	$\beta > -999$ (-999 is the NULL value)

on dE/dx points is used to ensure that selected tracks have sufficient energy loss information for particle identification purposes.

The identified particle analysis employs all cuts in 4 as well as those listed in 5. The Time-Of-Flight track cuts require that each track has a TOF match, that the TOF hit is within the nominal physical volume of the TOF tray and that the timing is valid. These cuts are used to require acceptable TOF information for use in particle identification. It should be noted that not all tracks matched to a TOF cell will have associated timing information for various reasons generally related to the electronics correction procedure. For this reason the $\beta > -999$ cut is required to ensure that we use only matched tof tracks that also have valid timing information.

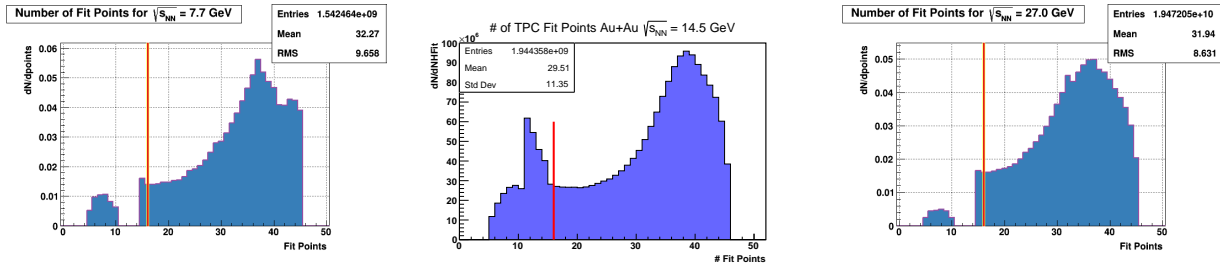


Figure 13: Number of fit points. Shown for $\sqrt{s_{NN}} = 7.7$ (left), 14.5 (center), and 27.0 (right) GeV.

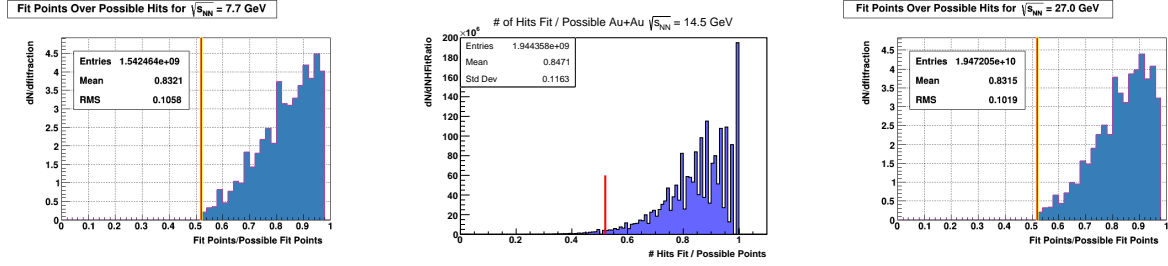


Figure 14: Number of fit points over the number of possible fit points. Shown for $\sqrt{s_{NN}} = 7.7$ (left), 14.5 (center), and 27.0 (right) GeV.

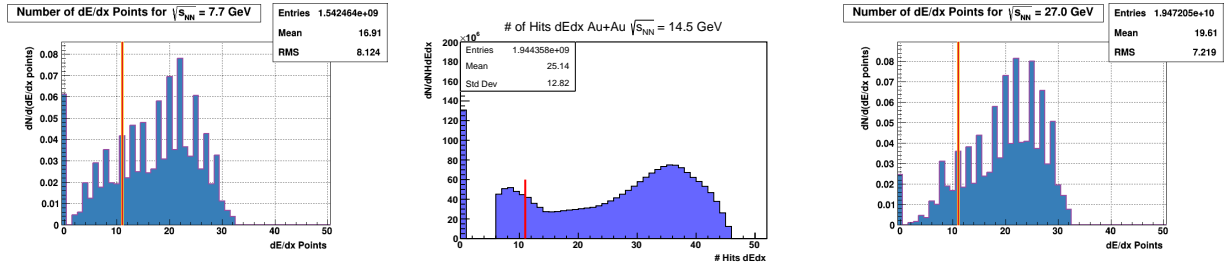


Figure 15: Number of dE/dx points. Shown for $\sqrt{s_{NN}} = 7.7$ (left), 14.5 (center), and 27.0 (right) GeV.

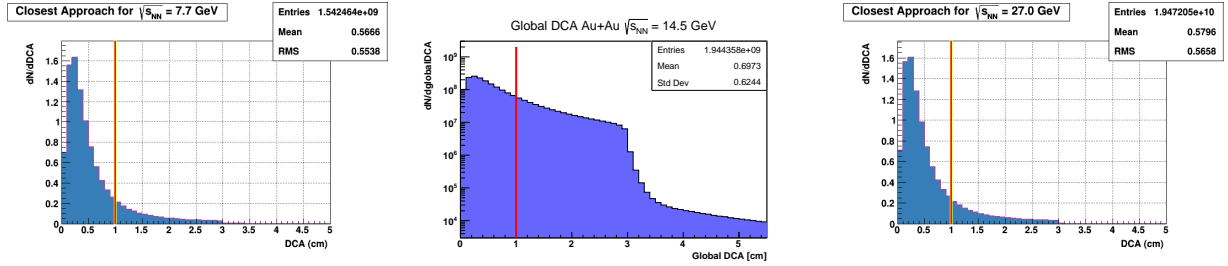


Figure 16: Distance to closest approach. Shown for $\sqrt{s_{NN}} = 7.7$ (left), 14.5 (center), and 27.0 (right) GeV.

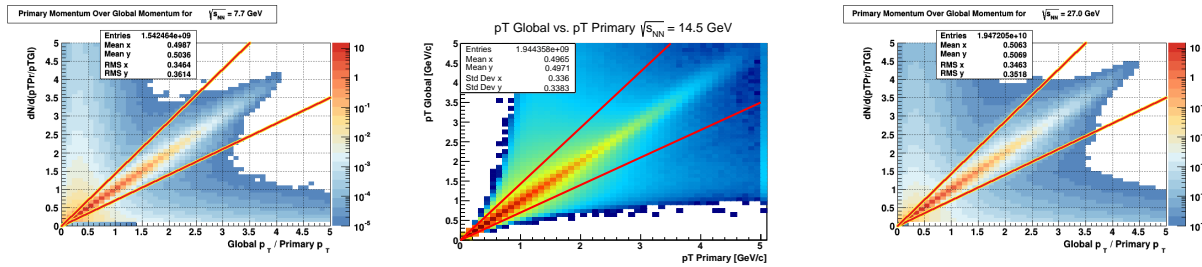


Figure 17: Global track p_T vs. primary track p_T . Shown for $\sqrt{s_{NN}} = 7.7$ (left), 14.5 (center), and 27.0 (right) GeV.

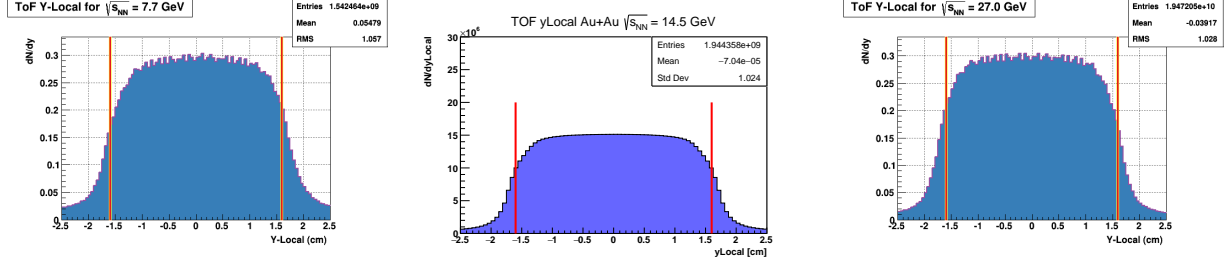


Figure 18: TOF yLocal hit position with cuts shown in red. Shown for $\sqrt{s_{NN}} = 7.7$ (left), 14.5 (center), and 27.0 (right) GeV.

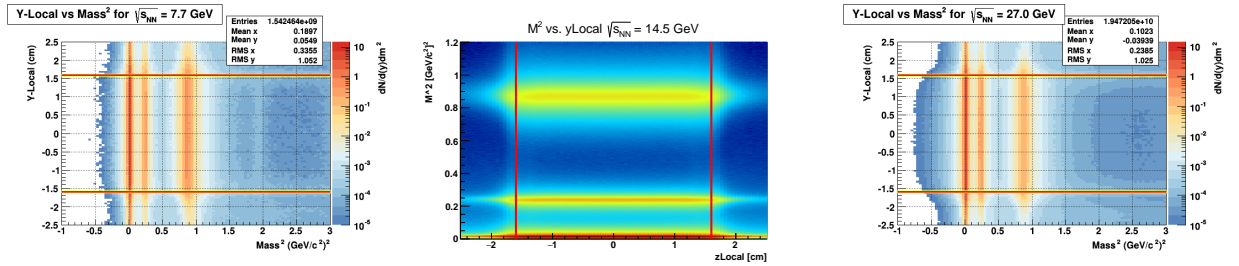


Figure 19: Mass squared vs. TOF yLocal hit position with cuts shown in red. Shown for $\sqrt{s_{NN}} = 7.7$ (left), 14.5 (center), and 27.0 (right) GeV.

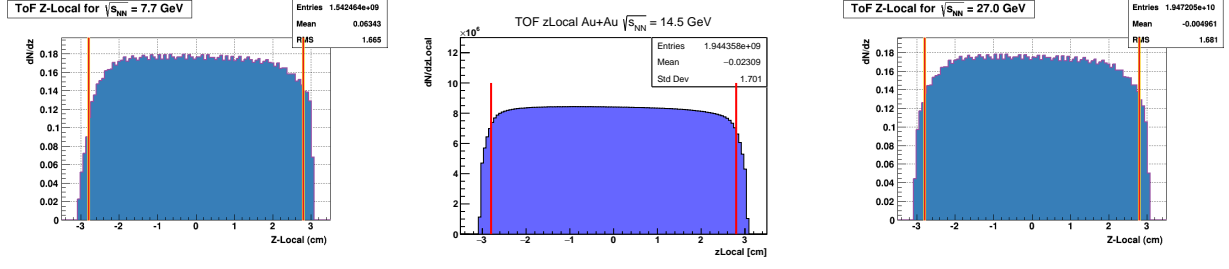


Figure 20: TOF zLocal hit position with cuts shown in red. Shown for $\sqrt{s_{NN}} = 7.7$ (left), 14.5 (center), and 27.0 (right) GeV.

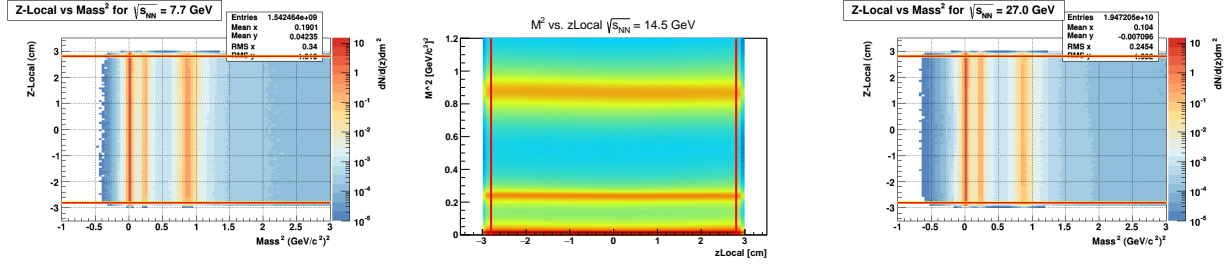


Figure 21: Mass squared vs. TOF zLocal hit position with cuts shown in red. Shown for $\sqrt{s_{NN}} = 7.7$ (left), 14.5 (center), and 27.0 (right) GeV.

4 Corrections

4.1 Feeddown, Knockout, and Photo-Production

When high- p_T particles pass through detector material, support material, and the beam pipe they sometimes knock out protons. These protons from secondary interactions form a background that needs to be subtracted from the data. While data-driven methods for this correction exist [31], they have been found to be consistent with a method using simulated events passed through a simulation of STAR that will be outlined in this section. The simulation is favored here because it simultaneously corrects for other backgrounds as well. One of these backgrounds is the photo-production of electrons in the same materials listed above. Another background comes from the weak decay of hadrons that carry strangeness and have a lifetime that separates their decay vertex from the primary vertex while still decaying within 1 m of the primary vertex. In order to subtract these backgrounds, UrQMD [32] produced collisions were run through a GEANT [33, 34] simulation of the STAR detector and then reconstructed. These simulated collisions were used to correct, at the ensemble level, for the fraction of background particles that would pass the track quality cuts used in this analysis. After the simulated events were made, the first step was filling histograms with tracks identified as pions, kaons and protons which were flagged as primary tracks. Then the ratio was taken between these histograms and histograms that were filled with all charged particles that passed the analysis track quality cuts. Each histogram was filled in a slice of $Mult$, 20 units broad, and binned in p_T . The next step was to fit these histograms with a 3 parameter function,

$$Correction_{feed}(p_T) = p_0 \cdot e^{-(p_1/p_T)^{p_2}}, \quad (3)$$

in each $Mult$ slice (Fig. 22), and then to fill histograms with these parameters in order to fit their centrality dependence (Fig. 23). With these fits for the $Mult$ dependence of the parameters of Eq. 3 it is possible to construct the $2D$ function,

$$Correction_{feed}(p_T, Mult) = (p_0 + p_1 \cdot Mult) \cdot e^{-((p_2 + p_3 \cdot Mult)/p_T)^{(p_4 + p_5 \cdot Mult)}}, \quad (4)$$

shown for $\sqrt{s_{NN}} = 7.7$ GeV/ c in Fig. 24. There are two advantages of constructing a $2D$ function for the feeddown correction rather than just fitting the p_T dependence in each centrality bin. The first advantage is that we leverage the functional form of the centrality dependence in order to reduce the number of simulated events needed. The second advantage is a more precise event by event correction rather than averaging across large centrality bins. Similar logic applies to the rest of the corrections in this chapter. Note that Fig. 24 exhibits a very weak centrality dependence so that this correction mostly cancels out in the ratio for R_{CP} .

4.2 Tracking Efficiency

The p_T and species dependent tracking efficiencies in the TPC were determined by embedding Monte Carlo tracks, modified by a GEANT [33, 34] simulation of STAR, into real events for each energy [35]. The embedding was done flat in $-1 < \eta < 1$ and flat in $0 < p_T <$

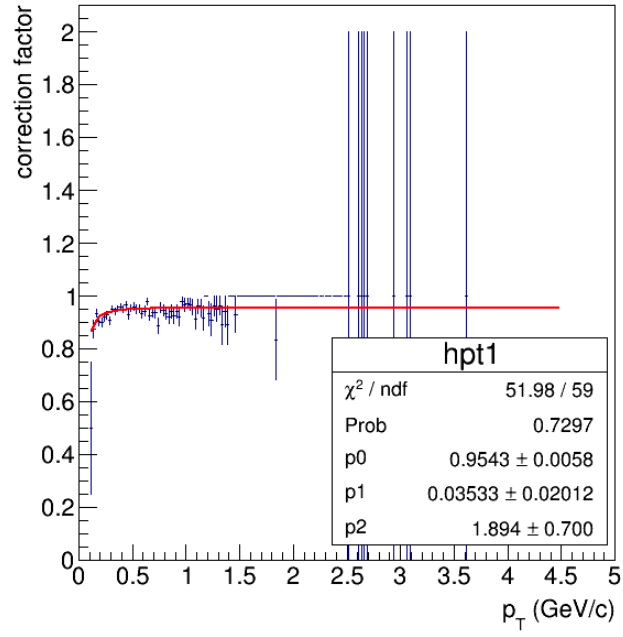


Figure 22: Fit of feeddown correction factor in $0 < Mult \leq 20$ at $\sqrt{s_{NN}} = 7.7$ GeV.

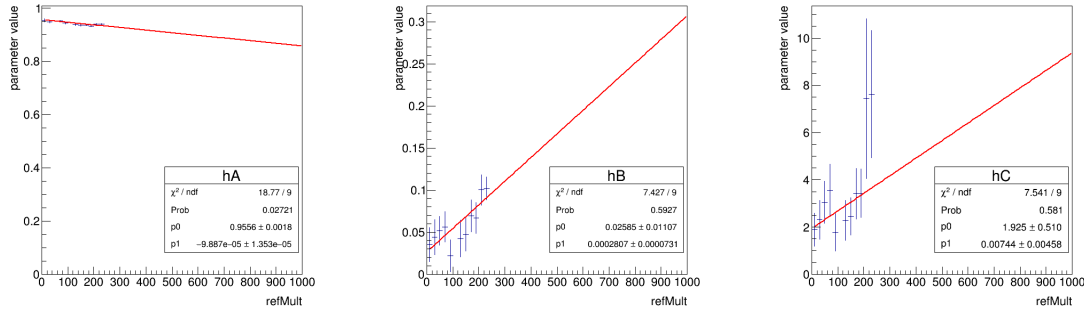


Figure 23: Linear fits of the $Mult$ dependence of parameters p_0 (a), p_1 (b), and p_2 (c) from Eq. 3 for $\sqrt{s_{NN}} = 7.7$ GeV.

5 GeV/ c in minimum bias events, with $\sim 500k$ embedded tracks per collision energy and species. The efficiency was defined to be the fraction of embedded Monte Carlo tracks that, after event reconstruction, were matched to reconstructed tracks that passed track quality cuts. Histograms of these efficiencies were filled with respect to p_T and in slices of $Mult$, similar to the histograms used for the feeddown correction. These p_T -dependent efficiencies, for each species and $Mult$ slice in the BES, were fit using, Eq. 5; while the efficiency corrected single species spectra were fit with Eq. 7.

$$\epsilon(p_T) = p_0 \cdot e^{-(p_1/p_T)^{p_2}} \quad (5)$$

Figure 25 shows a typical efficiency curve. The $Mult$ dependence of the parameters of 5 were fit with lines for p_0 and p_1 and with a power-law for p_2 (Fig. 26). Next, a 2D function was constructed for each species (i),

$$\epsilon_i(p_T, Mult) = (p_0 + p_1 \cdot Mult) \cdot e^{-((p_2 + p_3 \cdot Mult)/p_T)^{(p_4 \cdot Mult^{p_5})}}, \quad (6)$$

similar to what was done for the feed-down.

4.3 Identified Spectra Fits for Charged Hadron Analysis

The charged hadron efficiency is constructed as the weighted average of the single species efficiencies where the weights are provided by fits to the spectra,

$$spectra(p_T) = p_0 \cdot (1 - p_1 \cdot p_T^2)^{p_2}, \quad (7)$$

for each species. Other functional forms were tried but only this one gave consistently good fits across all centralities for all six species and the seven energies studied in this dissertation. Figure 28 shows a typical fit to the spectra. The centrality dependence of these parameters is then fit with power-laws for each of p_0 , p_1 and p_2 (Fig. 29). The identified spectra did not go as high in p_T as the unidentified spectra, but the efficiencies were nearly constant

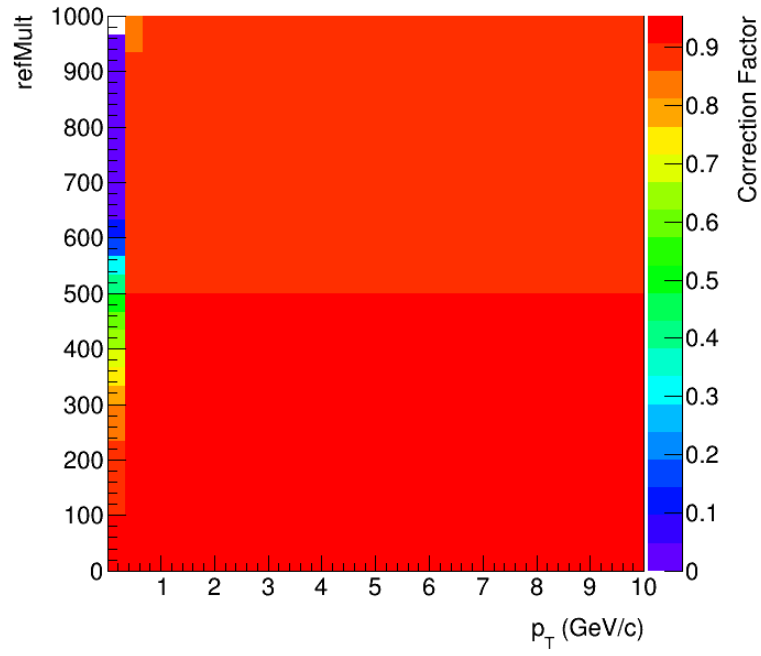


Figure 24: Feeddown correction used for $\sqrt{s_{NN}} = 7.7$ GeV.

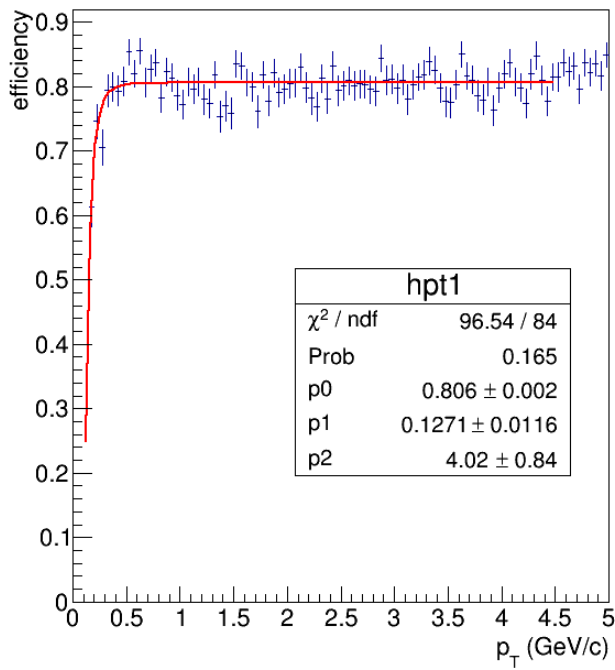


Figure 25: Fit of single species efficiency from embedding of π^+ into peripheral 60-80% centrality of $\sqrt{s_{\text{NN}}} = 7.7$ GeV.

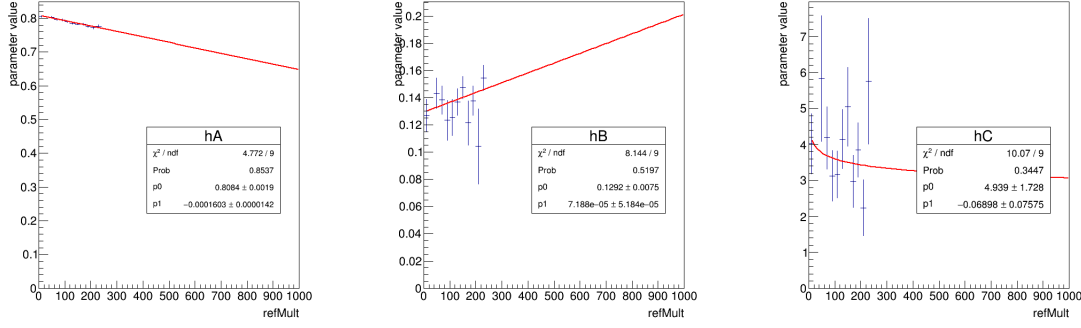


Figure 26: Spectra with fits for central 0-5% $\sqrt{s_{\text{NN}}} = 7.7$ GeV π^+ (a), p (b), K^+ (c), π^- (d), \bar{p} (e), and K^- (f).

in the p_T region extrapolated into, which limited the impact from the extrapolation on the systematic uncertainties. Next a 2D function was constructed,

$$\text{spectra}_i(p_T, \text{Mult}) = (p_0 \cdot \text{Mult}^{p_1}) \cdot (1 - p_2 \cdot \text{Mult}^{p_3} \cdot p_T^2)^{p_4 \cdot \text{Mult}^{p_5}}, \quad (8)$$

for each species, i (Fig. 30).

4.4 Momentum Resolution and Energy Loss

Reconstructed tracks do not exactly match the true path that a particle followed. This means that the reconstructed p_T of a particle can deviate from the actual p_T the particle had immediately after a collision. One reason for this is that TPC hits have a resolution associated with their position. Using the positions of these hits given by the TPC readout to reconstruct tracks means that errors in the position of the hits result in tracks that describe inaccurate trajectories and curvatures. This results in an imperfect momentum resolution. The momentum resolution can be improved by requiring more hits per track, by narrowing the cut on DCA, and by using the reconstructed primary vertex position in the track reconstruction. Figure 31 shows the distributions of relative p_T shifts of embedded tracks. Within p_T bins these distributions are projected onto the y-axis and fit with Gaussians as in Fig. 32. The means give the energy loss correction while the Gaussian widths give the momentum resolutions. The momentum dependence of the Gaussian width is fit at high p_T , while avoiding the edges of the histogram as seen in Fig. 33, in order to extrapolate to higher p_T where no embedding was done. In order to estimate the effect of momentum resolution on the reconstructed spectra several steps are taken. First the spectra are fit. Then one histogram is filled by random sampling this fit and another by random sampling the fit and smearing the momentum. The ratios of the smeared to the non-smeared distributions give an estimate for how large the effect of momentum resolution is on the spectra. 100M tracks are generated for each histogram. The histograms are primarily filled at low p_T due to how steeply the spectra fall. Figure 34 shows that momentum smearing has a negligible effect at low p_T but we want to be certain of the behavior at high p_T so the fit in Fig. 33 is extrapolated to high p_T and the spectra is sampled in this higher p_T region using the same

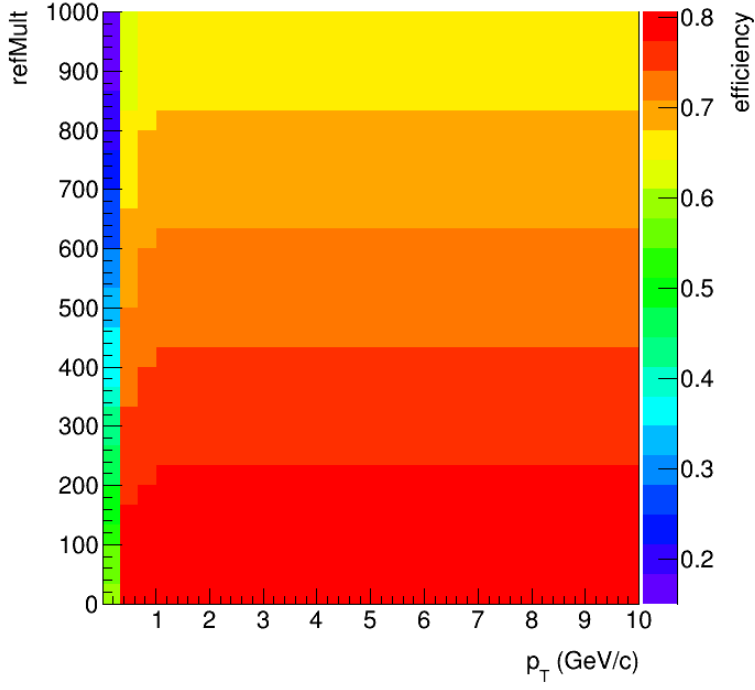


Figure 27: Fit of single species efficiency from embedding of π^+ for $\sqrt{s_{\text{NN}}} = 7.7$ GeV.

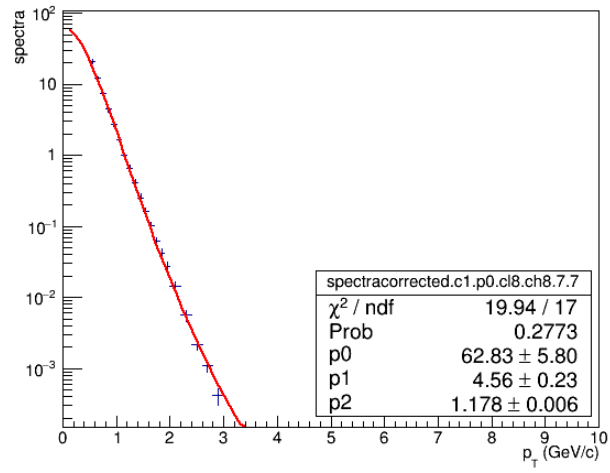


Figure 28: Single species efficiencies of π^+ , p , K^+ , π^- , \bar{p} , and K^- for central 0-5% $\sqrt{s_{\text{NN}}} = 7.7$ GeV.

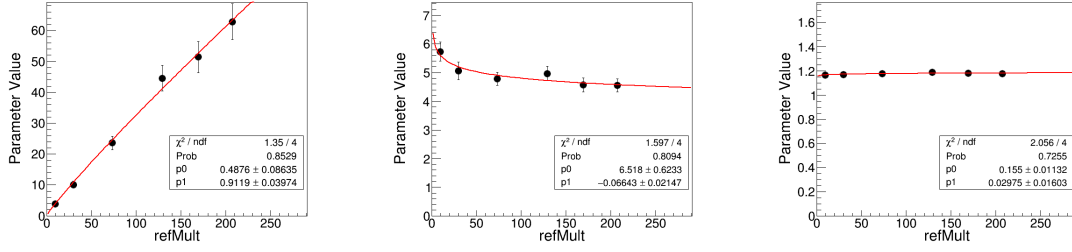


Figure 29: Spectra with fits for central 0-5% $\sqrt{s_{\text{NN}}} = 7.7$ GeV π^+ (a), p (b), K^+ (c), π^- (d), \bar{p} (e), and K^- (f).

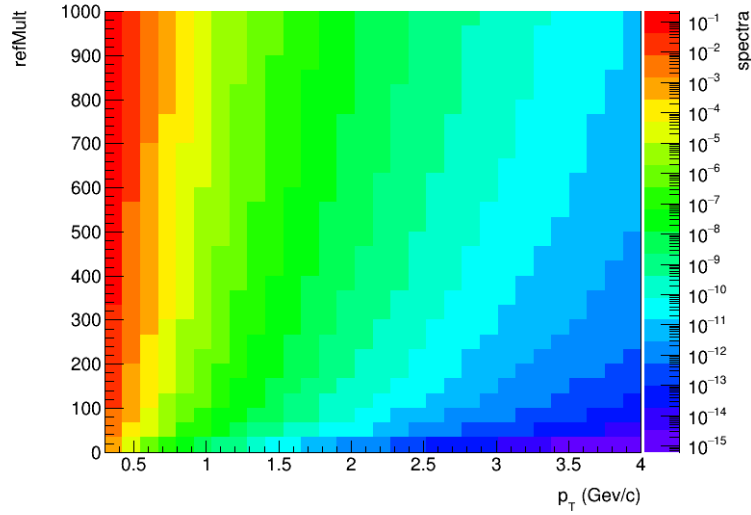


Figure 30: Single species efficiencies of π^+ , p , K^+ , π^- , \bar{p} , and K^- for central 0-5% $\sqrt{s_{\text{NN}}} = 7.7$ GeV.

method as before. The result of this procedure is shown in Fig. 35 where we see a 1% effect. Because the correction is negligible at low p_T and small at high p_T it is not applied and is instead included in the systematic uncertainty analysis for the high- p_T charged hadrons.

4.5 Combined Correction for Charged Hadron Analysis

The final step is to construct the correction factor that includes the feed-down correction as well as the charged hadron efficiency. The previously constructed 2D functions are combined for each collision energy:

$$\text{correction}(p_T, \text{Mult}) = \text{Correction}_{\text{feed}} \frac{\sum_i \epsilon_i \cdot \text{spectra}_i}{\sum_i \text{spectra}_i}. \quad (9)$$

Each charged track is weighted by the inverse of this combined correction. The corrections for each collision energy are shown in Fig. 36.

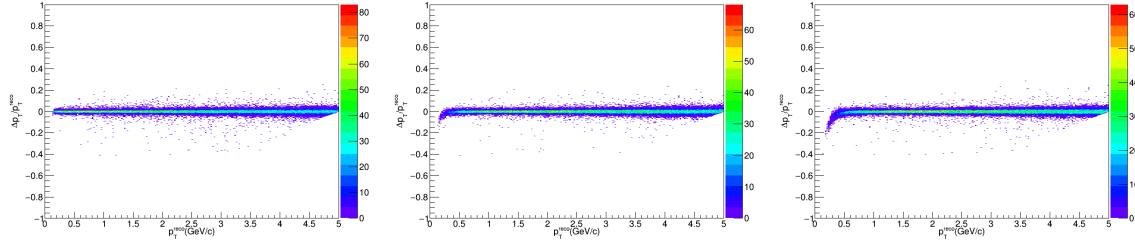


Figure 31: Distributions of relative p_T shifts for embedded π^+ (a), K^+ (b), and p (c) particles at $\sqrt{s_{NN}} = 7.7$ GeV.

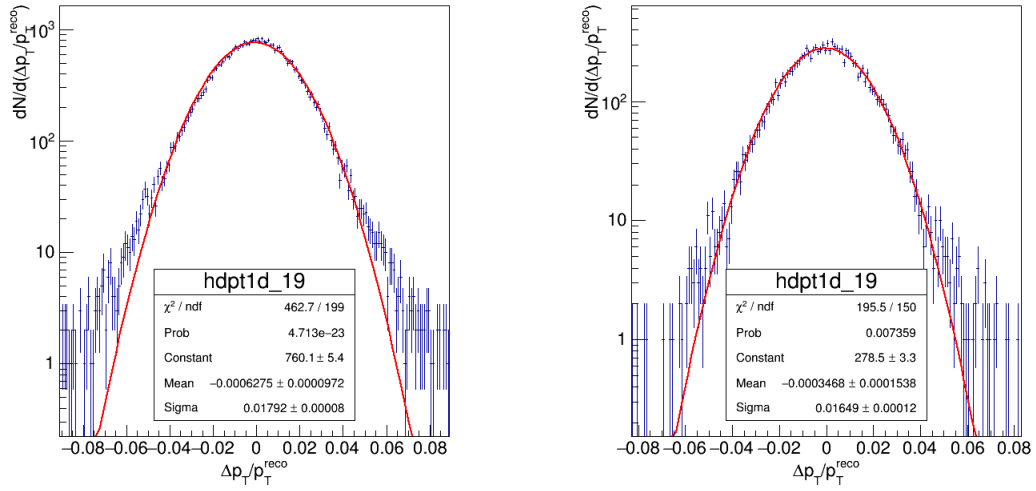


Figure 32: The relative momentum shift distributions for $\sqrt{s_{NN}} = 7.7$ and 62.4 GeV in $4.5 < p_T < 4.75$ GeV/c.

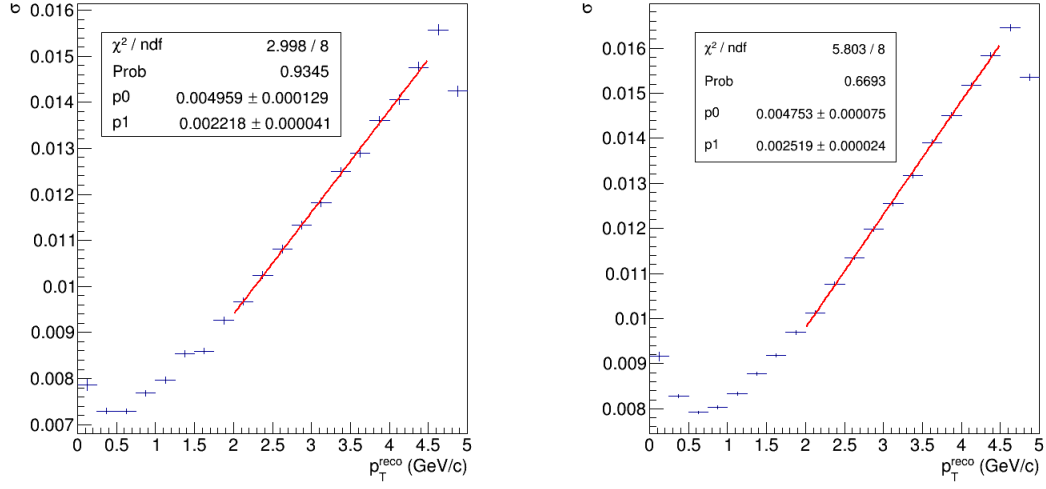


Figure 33: Momentum resolution as a function of p_T and fit at high- p_T with a linear fit for π^+ at $\sqrt{s_{NN}} = 7.7$ GeV and 62.4 GeV. The momentum resolution is similar for the other species and energies.

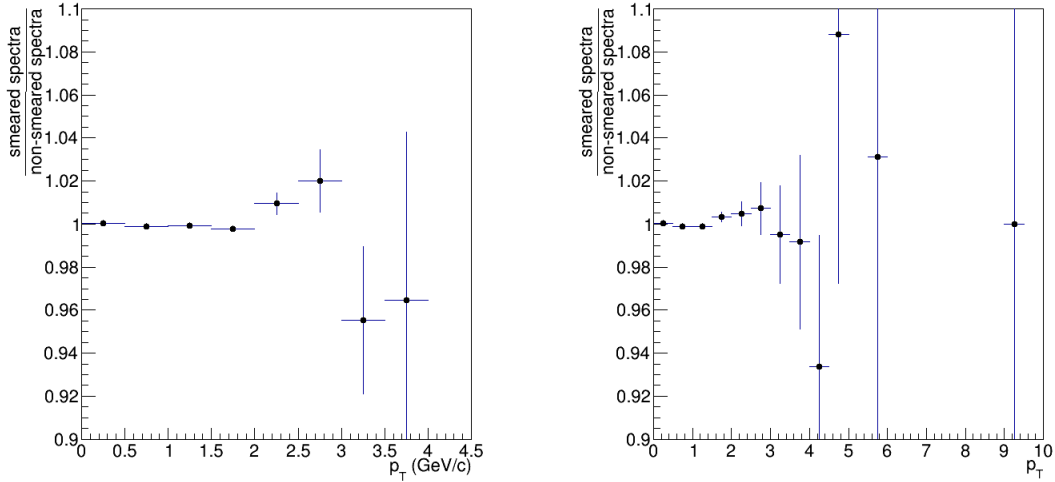


Figure 34: Ratio of smeared spectra to non-smeared spectra as a function of p_T for π^+ at $\sqrt{s_{NN}} = 7.7$ GeV and 62.4 GeV.

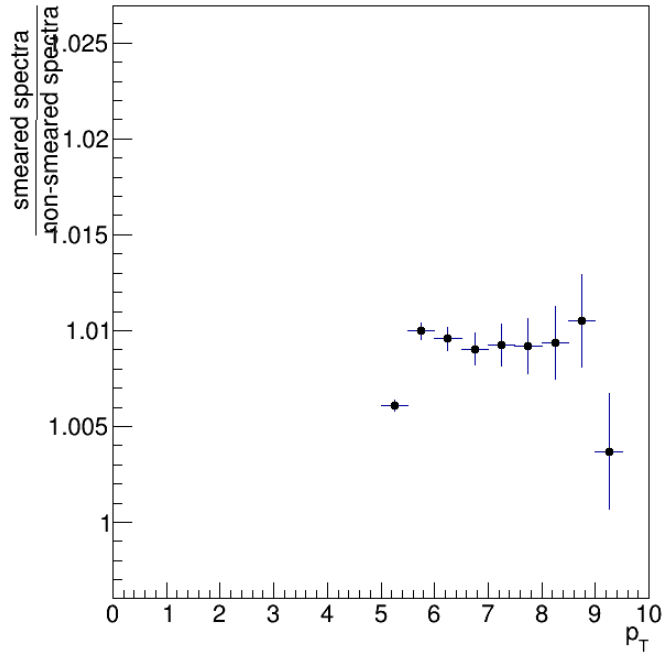
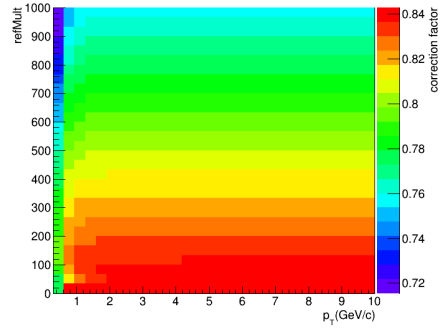
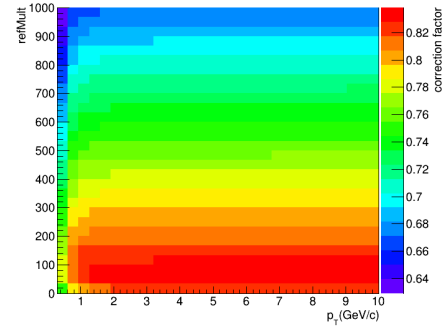


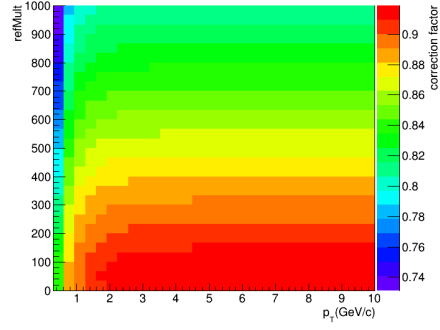
Figure 35: Ratio of smeared spectra to non-smeared spectra as a function of p_T for high- p_T π^+ particles at $\sqrt{s_{NN}} = 62.4$ GeV.



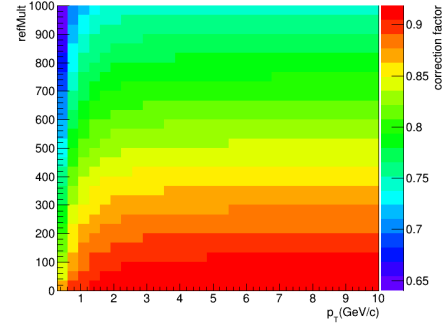
(a) 7.7 GeV



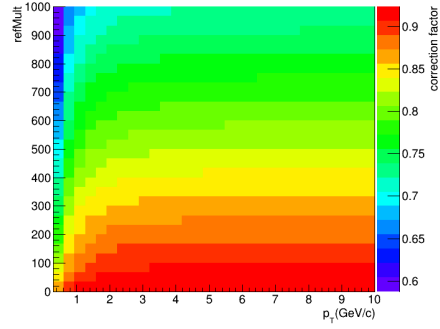
(b) 11.5 GeV



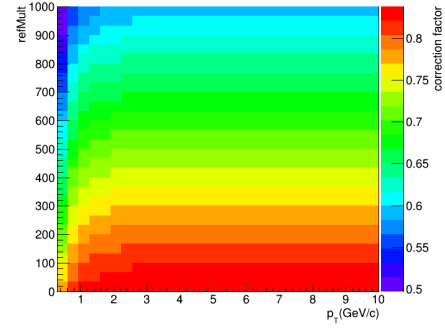
(c) 14.5 GeV



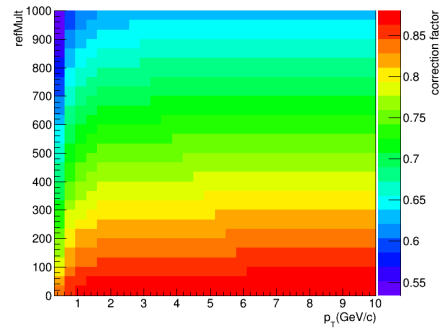
(d) 19.6 GeV



(e) 27 GeV



(f) 39 GeV



(g) 62.4 GeV

Figure 36: Combined correction factors for efficiency, feeddown, and knockout for each energy.

5 Analysis Details : Identified Particle Spectra

The analysis of the π , K, p spectra consists of several major steps. These steps are organized into 3 main categories: 1) determining corrections from embedding, 2) identified particle yield extraction, and 3) feeddown corrections.

Data Reduction: All analysis procedures outlined in this note begin by reducing and normalizing the input data. The embedding and feeddown procedures use standard STAR MiniMC files while the yield extraction step uses standard STAR MuDst files. The data reduction step applies bad run rejection (see Section 3.1), event cuts (see Section 3.2) and a loosened set of track cuts (see Section 3.4). Loosened track cuts are applied at this stage so that a single dataset can be used for the main analysis and for track-cut systematic studies. The normalized dataset produced in the data reduction step will be referred to as “SpectraPicoDst” throughout the note.

5.1 Particle Identification

5.1.1 Measurement Recentering

The TPC and TOF detectors are used in this analysis to identify particle species. The TPC provides dE/dx and the TOF provides $1/\beta$ as seen in Fig. 38. These quantities depend on the particle mass $dE/dx \propto (z^2/\beta^2) \ln(\beta\gamma)$ and $1/\beta \propto (m_0\gamma)/p$ and are therefore useful for separating particle species.

In this analysis these two observables are combined to maximize the separation power and stability of the yield extraction. For this procedure the measured dE/dx and $1/\beta$ are re-weighted to account for poor detector calibrations, finite bin-width effects, momentum resolution effects, and for normalization using :

$$z' = \Sigma_s [w_s(z) \times (z + \mu^s(\langle p \rangle) - \mu^s(p))] - \mu^h(\langle p \rangle) \quad (10)$$

where h is the species that should be centered at $z' = 0$, s is the species index (e.g. π , K, p), w_s is a weight given to each species as a function of the measurement, p is the track momentum in GeV/c, $\langle p \rangle$ is the average momentum in the given p_T (momentum in the plane transverse to the beam-line) and y (a measure of the particle’s velocity in the direction of the beam-line) range, $\mu^s(p)$ is the theoretical mean for the measurement at the given momentum value, and z is the measured value, either dE/dx or $1/\beta$. See Fig. 39 for an example of the simultaneous recentering. These two variables are then used simultaneously in a χ^2 minimization fit to extract particle yields as a function of p_T . This procedure is discussed in more detail in the next section.

Throughout the rest of the note the terms “ z_b ” and “ z_d ” will be used to refer the re-centered $1/\beta$ and $\ln(dE/dx)$ values respectively.

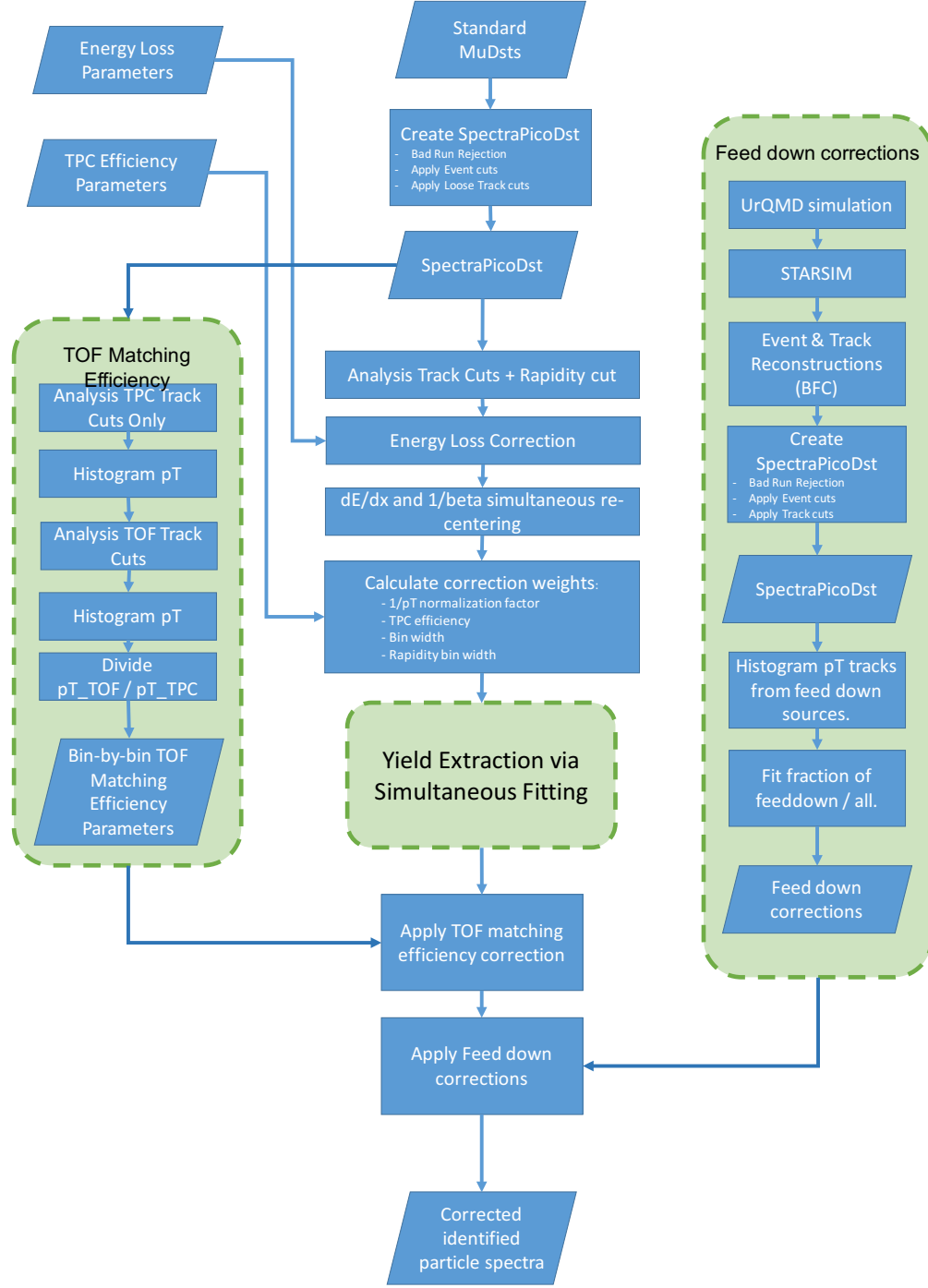


Figure 37: Flowchart of analysis procedure.

5.1.2 Simultaneous Gaussian fit

In order to extract the particle yields, first the full 2D z_b vs. z_d dataset is reduced into eight 1D distributions. The first two of these eight distributions are the 1D projections of

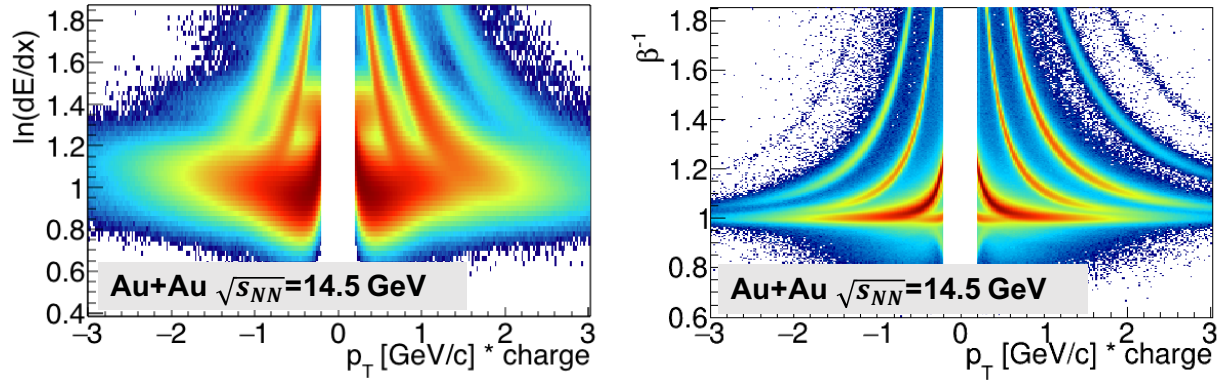


Figure 38: The measured $\ln(dE/dx)$ versus $p_T \times \text{charge}$ from the TPC (left). The measured velocity expressed at $1/\beta$ versus $p_T \times \text{charge}$ from the TOF (right). The bands correspond to particles of different masses.

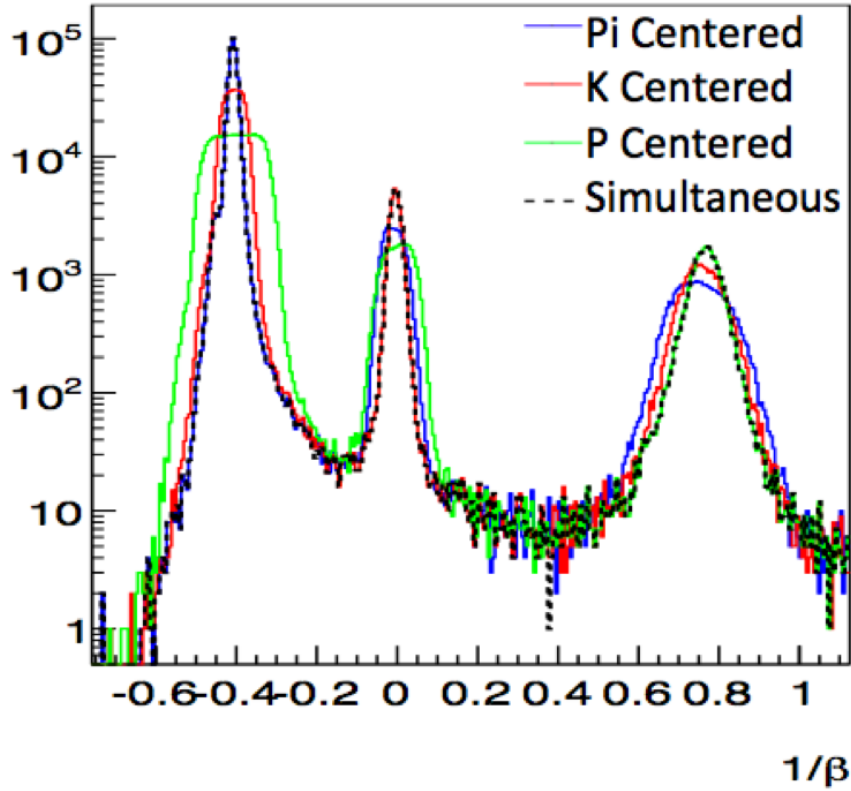


Figure 39: Example of the simultaneous re-centering procedure in a single p_T bin. This example compares the traditional re-centering procedure for π , K, p and the simultaneous re-centering procedure.

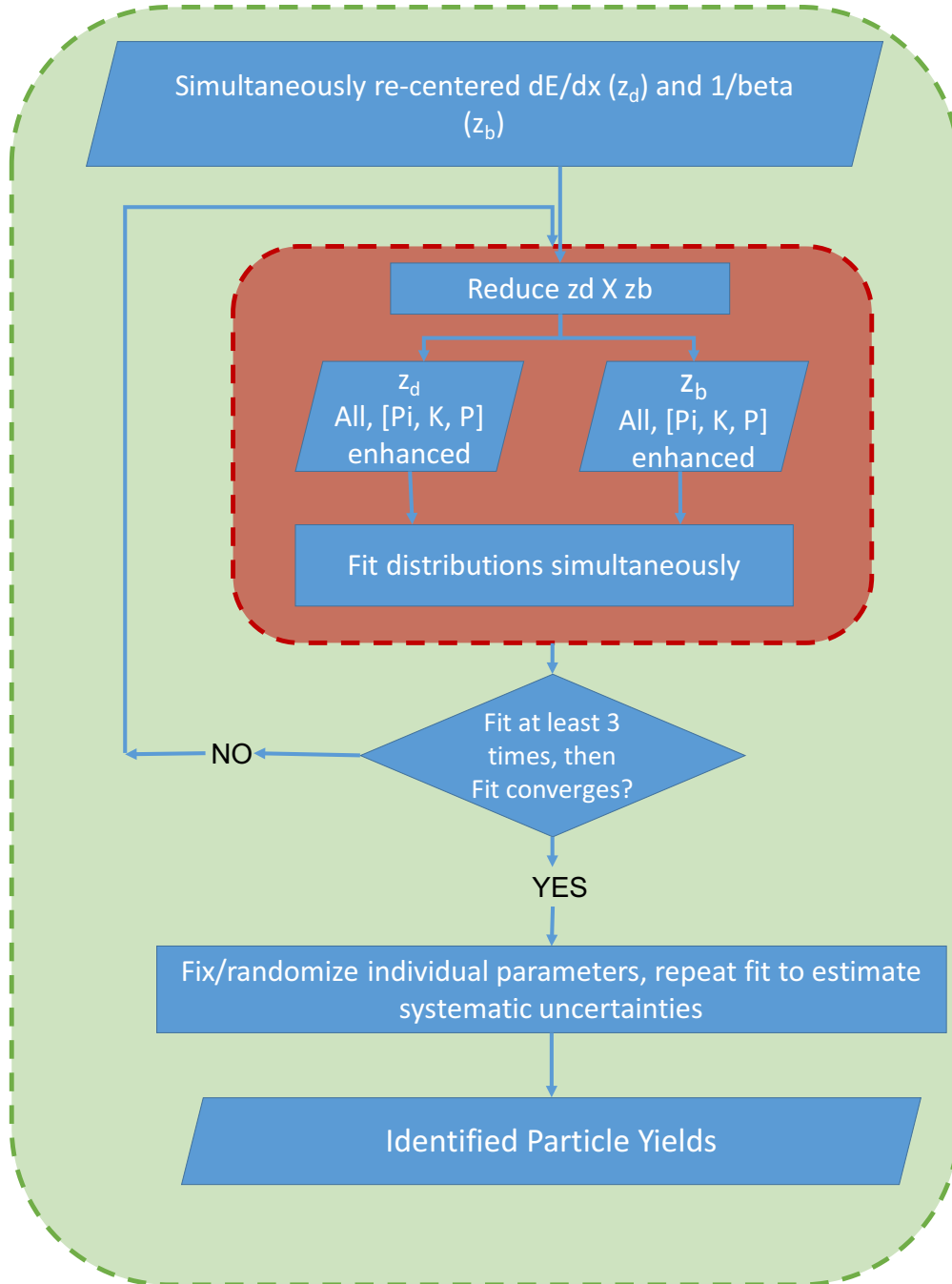


Figure 40: Flowchart of procedure used for determining the energy loss and TPC efficiency and acceptance corrections.

307 all tracks onto the z_d and z_b axes respectively. Six more distributions are formed (three from
 308 z_b projections and three from z_d projections) by applying a 2σ cut on $z_d(z_b)$ around the particle
 309 of interest (one of π , K, p) and then projecting onto the $z_b(z_d)$ axis. These six projections
 310 are distributions with relative enhancements in the yield of the particle of interest. Fitting

all eight of these distributions simultaneously allows for the majority of the full 2D $z_d \times z_b$ dataset to be used while minimizing the computational intensity of the fit. All eight of the z_b and z_d distributions are each fit with a function of the following form:

$$f(x) = \frac{Y_\pi}{\sigma_\pi \sqrt{2\pi}} e^{-\frac{1}{2} \left(\frac{x - \mu_\pi}{\sigma_\pi} \right)^2} + \frac{Y_K}{\sigma_K \sqrt{2\pi}} e^{-\frac{1}{2} \left(\frac{x - \mu_K}{\sigma_K} \right)^2} + \frac{Y_p}{\sigma_p \sqrt{2\pi}} e^{-\frac{1}{2} \left(\frac{x - \mu_p}{\sigma_p} \right)^2} \quad (11)$$

where x can be either z_b or z_d . Table 6 shows the full list of variables used for a single fit. As outlined in Figure 42, the yield extraction procedure recursively fits and reduces the data to ensure that yield extraction converges with significant stability. The main steps in the fitting procedure are as follows :

1. Load data (simultaneously re-centered z_b and z_d).
2. Reduce z_b and z_d into eight 1D projections.
3. Setup fit models and variables.
4. Maximum likelihood fit
5. Repeat steps 2 - 4 at least three times to ensure a stable fit. Then repeat until fit reaches stable convergence.
6. Randomize individual parameters (fixing others) to explore systematic uncertainties in fitting procedure.
7. Report particle yields and uncertainties.

This procedure is followed for each particle species (π , K, p), for positive and negative charges, for each centrality bin, and for each p_T bin. z

Table 6: Unique Variables in Fit

Variable Name	Description
$\mu_{z_b}^{\pi,K,p}$	Center of z_b Gaussian distribution for π , K , p respectively (shared)
$\mu_{z_d}^{\pi,K,p}$	Center of z_d Gaussian distribution for π , K , p respectively (shared)
$\sigma_{z_b}^{\pi,K,p}$	Sigma of z_b Gaussian distribution for π , K , p respectively (shared)
$\sigma_{z_d}^{\pi,K,p}$	Sigma of z_d Gaussian distribution for π , K , p respectively (shared)
$Y^{\pi,K,p}$	Normalized Yield of Gaussian distributions for π , K , p respectively (shared)
$Y_{z_b,\pi}^{\pi,K,p}$	Normalized Yield of Gaussian distributions for π , K , p respectively, in the $z_b\pi$ enhanced distribution
$Y_{z_b,K}^{\pi,K,p}$	Normalized Yield of Gaussian distributions for π , K , p respectively, in the z_bK enhanced distribution
$Y_{z_b,p}^{\pi,K,p}$	Normalized Yield of Gaussian distributions for π , K , p respectively, in the z_bp enhanced distribution
$Y_{z_d,\pi}^{\pi,K,p}$	Normalized Yield of Gaussian distributions for π , K , p respectively, in the $z_d\pi$ enhanced distribution
$Y_{z_d,K}^{\pi,K,p}$	Normalized Yield of Gaussian distributions for π , K , p respectively, in the z_dK enhanced distribution
$Y_{z_d,p}^{\pi,K,p}$	Normalized Yield of Gaussian distributions for π , K , p respectively, in the z_dp enhanced distribution

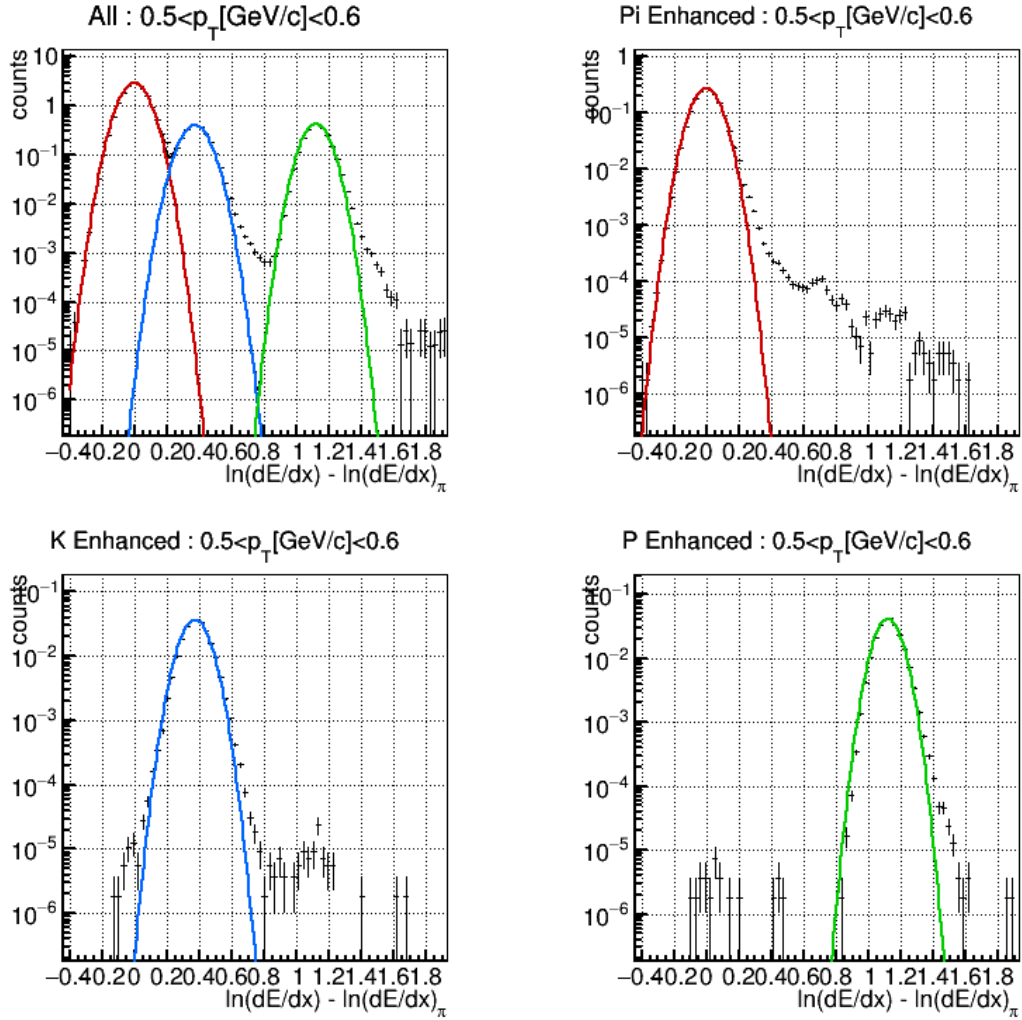


Figure 41: The four 1D z_d distributions: The unenhanced (all tracks) distribution (top-left), Pion enhanced (top-right), Kaon enhanced (bottom-left), and Proton enhanced (bottom-right). Fits are shown in red (π), blue (K), and green (p).

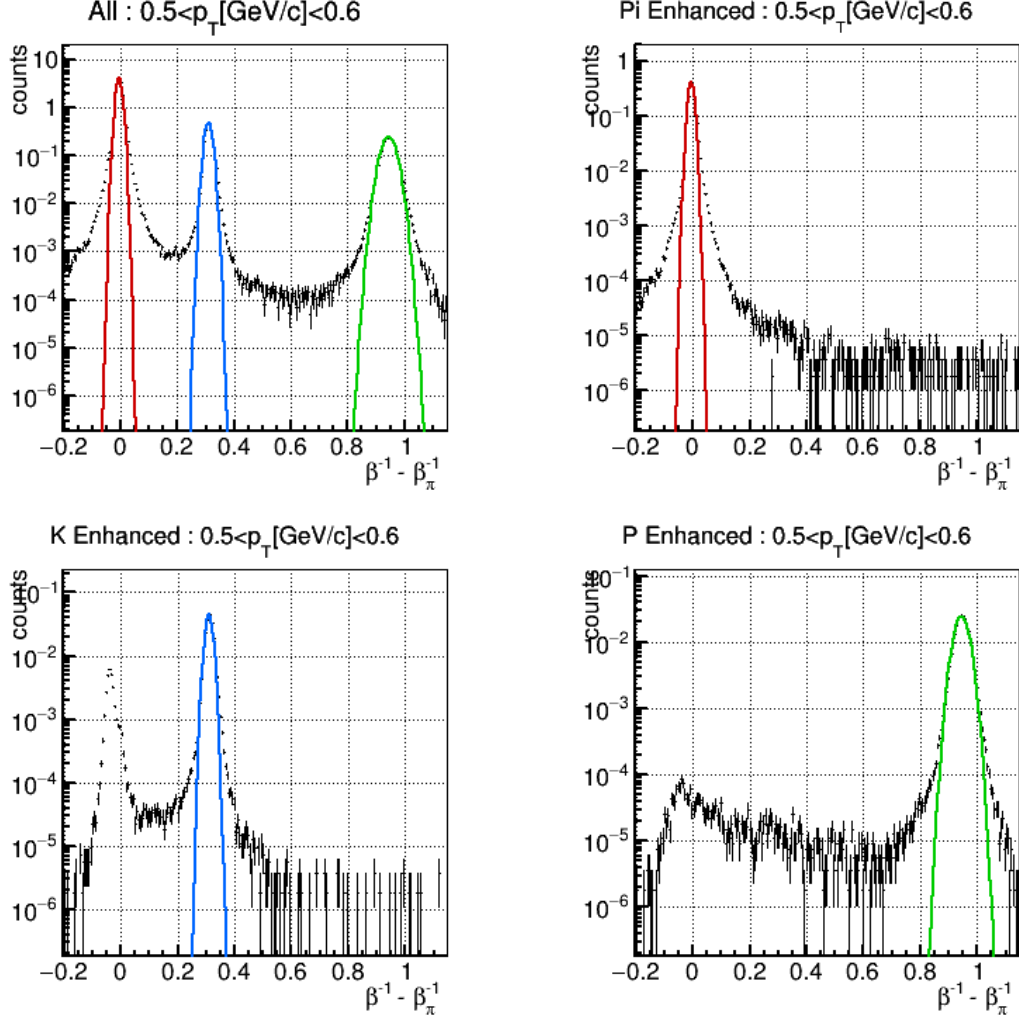


Figure 42: The four 1D z_b distributions: The unenhanced (all tracks) distribution (top-left), Pion enhanced (top-right), Kaon enhanced (bottom-left), and Proton enhanced (bottom-right). Fits are shown in red (π), blue (K), and green (p).

5.2 Efficiency Corrections

5.2.1 TPC Track Reconstruction Efficiency and Acceptance

This analysis uses primary tracks reconstructed in the TPC. The track reconstruction algorithms take raw hits in the TPC and attempt to reconstruct physical track helices. This procedure has inefficiencies due to detector limitations and physical effects. The efficiency of track reconstruction and acceptance can be parameterized in terms of kinematic variables and then used to correct the raw yield extraction. The efficiency and acceptance correction are parameterized for each particle species and charge in bins of p_T and centrality. Since this analysis uses a fairly small range in mid-rapidity ($-0.25 < y < 0.25$) these corrections are binned in a single rapidity bin.

The TPC track reconstruction efficiency and acceptance corrections are determined using the standard STAR MiniMC files from embedding. The main steps in this procedure, shown in Figure 43, are as follows :

1. Create SpectraPicoDst files from MiniMC files. This step applies event and loosened track cuts. This step also applies bad-run rejection since some embedding data incorrectly included bad-runs.
2. Apply analysis track cuts
3. Produce histograms of p_T for MC (MonteCarlo) tracks for each species, charge, and centrality.
4. Produce histograms of p_T for matched RC (ReConstructed) tracks for each species, charge, and centrality.
5. Divide RC p_T distribution by corresponding MC p_T distribution using binomial errors (TGraphAsymmErrors::BayesDivide)
6. Fit efficiency histograms to $f(p_T) = ae^{(-b/p_T)^c}$ and calculate confidence level of fits.
7. Export efficiency parameters.

These efficiency corrections are applied on a track-by-track basis by evaluating the efficiency fit at a given track's p_T . The track-by-track correction factors are used to determine the correction factor for the given p_T bin and applied after the yield extraction fit. As a consistency check the analysis can also be run so that the efficiency for an entire p_T bin is calculated at the bin-center and applied to the whole bin.

5.2.2 TOF Track Matching Efficiency

The TOF track cuts reject a significant number of tracks reconstructed by the TPC that do not have a corresponding hit in the TOF electronics. For this reason corrections must be applied to account for the TOF track cuts.

The TOF track matching efficiency corrections are calculated using a data-driven method.
The TOF track matching efficiency is defined as:

$$\epsilon_{\text{TOF}}(p_T) = \frac{\text{tracks}_{\text{TOF+TPC}}}{\text{tracks}_{\text{TPC}}} \quad (12)$$

This is calculated separately for each of the particles of interest (π , K, p), for each charge, and in each centrality bin using the following procedure:

1. Histogram for each centrality the primary track p_T for tracks passing TPC track ($\text{track}_{\text{TPC}}$) cuts and with an $|\text{n}\sigma_{\text{dE/dx}}^h| < 2.0$, where h corresponds to either π , k, or p .
2. Histogram for each centrality the primary track p_T for tracks passing TPC and TOF track cuts ($\text{track}_{\text{TOF+TPC}}$) and with an $|\text{n}\sigma_{\text{dE/dx}}^h| < 2.0$, where h corresponds to either π , k, or p .
3. Divide the p_T distributions of ($\text{track}_{\text{TPC}}$) and ($\text{track}_{\text{TOF+TPC}}$).

The efficiency parameters for TOF are not fit to a fit function. Instead the correction parameters are applied bin-by-bin in the same binning in which the yields are extracted.

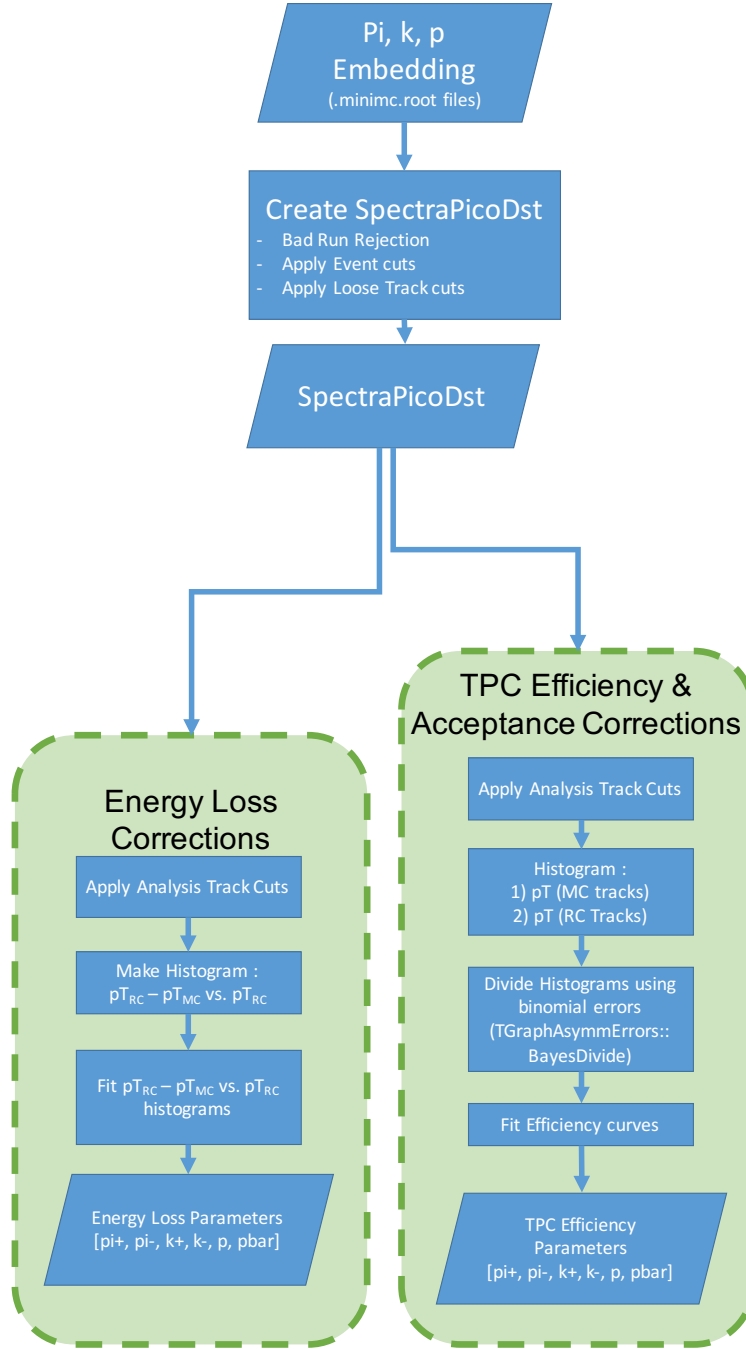


Figure 43: Flowchart of procedure used for determining the energy loss and TPC efficiency and acceptance corrections.

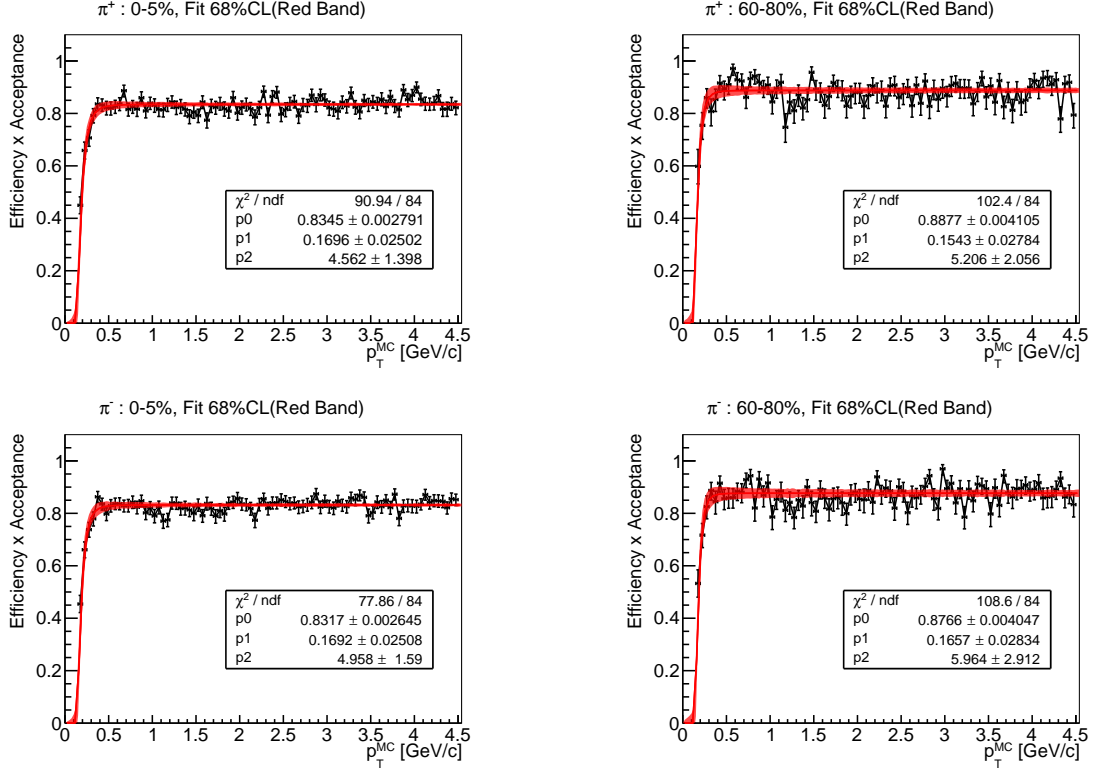


Figure 44: Efficiencies for π^+ (top row) and π^- (bottom row) for 0-5% centrality (left column) and 60-80% centrality (right column) in Au+Au collisions at $\sqrt{s_{NN}} = 14.5$ GeV. Red line shows nominal fit while red band shows the 68% confidence level calculated from the fit's covariance matrix.

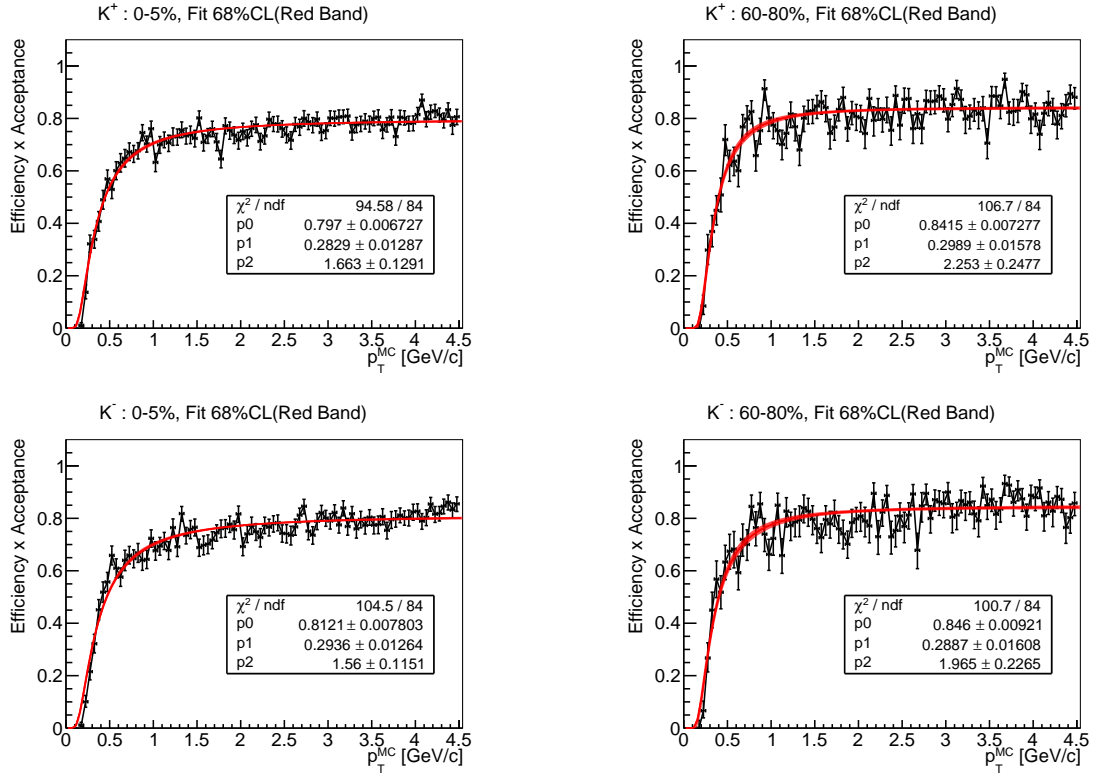


Figure 45: Efficiencies for K^+ (top row) and K^- (bottom row) for 0-5% centrality (left column) and 60-80% centrality (right column) in Au+Au collisions at $\sqrt{s_{NN}} = 14.5$ GeV. Red line shows nominal fit while red band shows the 68% confidence level calculated from the fit's covariance matrix.

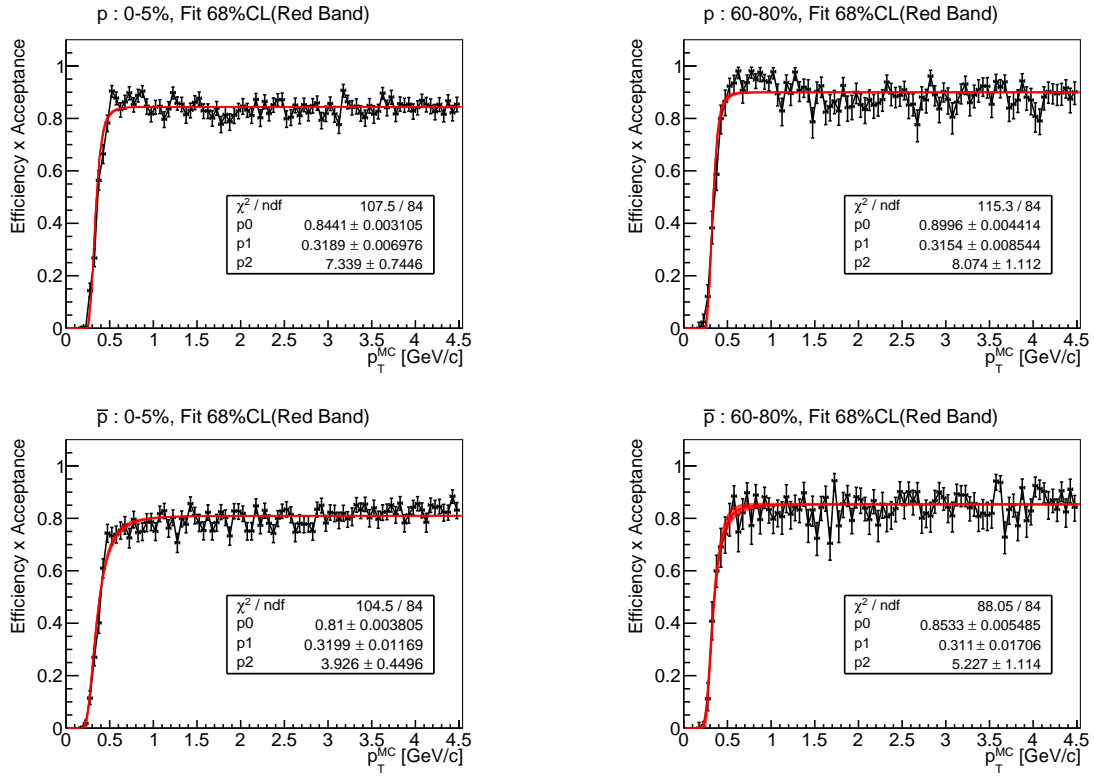


Figure 46: Efficiencies for p (top row) and \bar{p} (bottom row) for 0-5% centrality (left column) and 60-80% centrality (right column) in Au+Au collisions at $\sqrt{s_{NN}} = 14.5$ GeV. Red line shows nominal fit while red band shows the 68% confidence level calculated from the fit's covariance matrix.

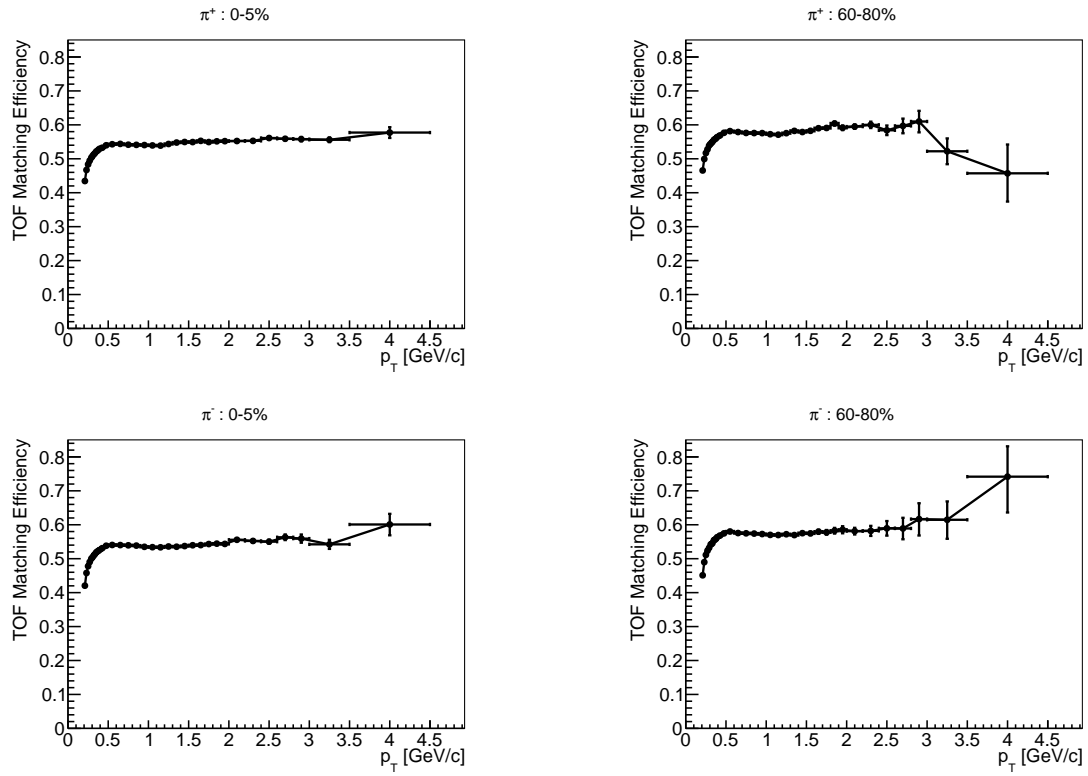


Figure 47: Data driven TOF Efficiencies for π^+ (top row) and π^- (bottom row) for 0-5% centrality (left column) and 60-80% centrality (right column) in Au+Au collisions at $\sqrt{s_{NN}} = 14.5$ GeV.

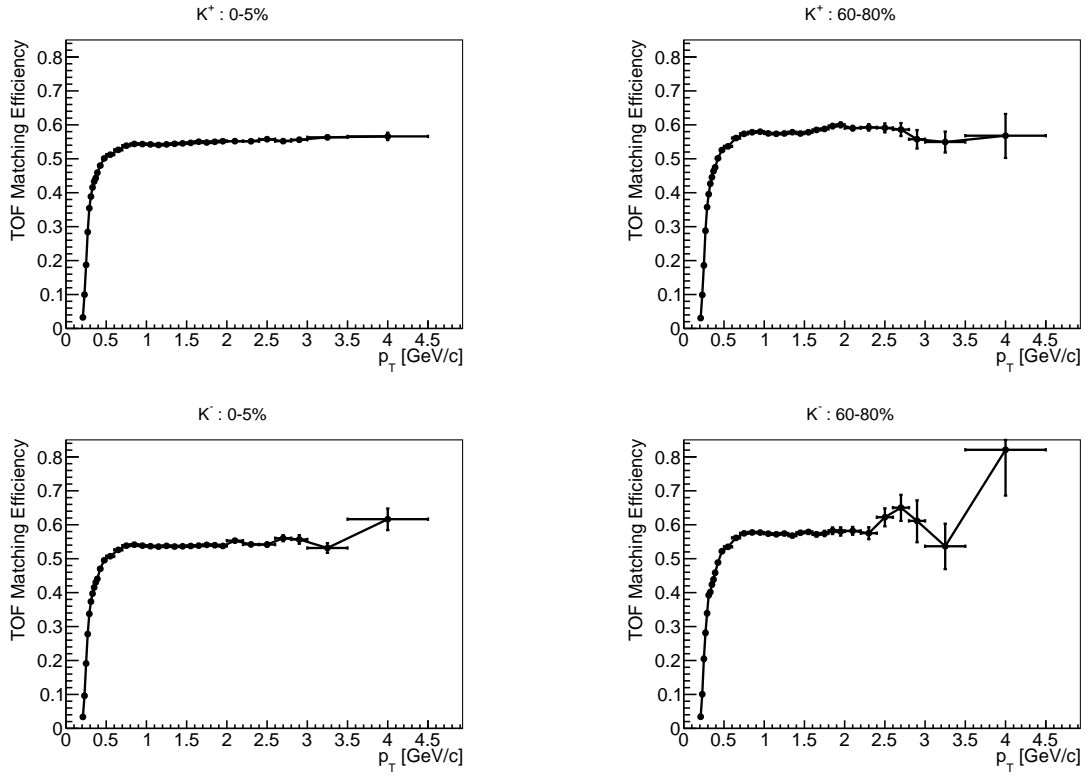


Figure 48: Data driven TOF Efficiencies for K^+ (top row) and K^- (bottom row) for 0-5% centrality (left column) and 60-80% centrality (right column) in Au+Au collisions at $\sqrt{s_{NN}} = 14.5$ GeV.

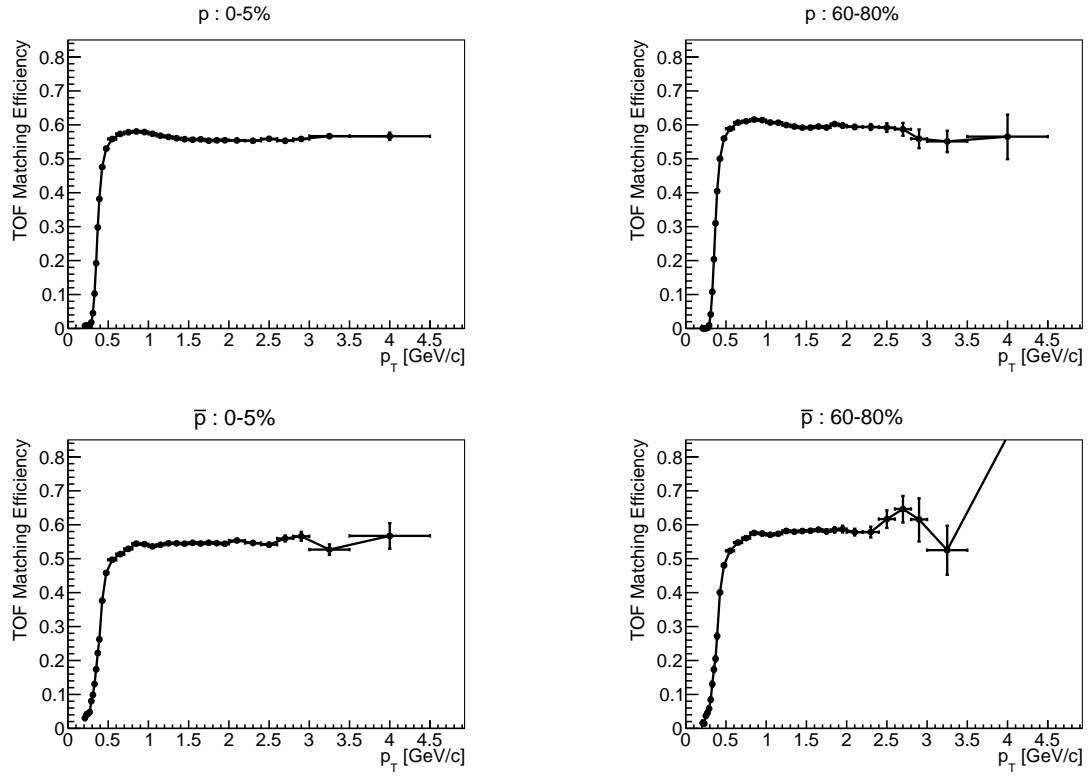


Figure 49: Data driven TOF Efficiencies for p (top row) and \bar{p} (bottom row) for 0-5% centrality (left column) and 60-80% centrality (right column) in Au+Au collisions at $\sqrt{s_{NN}} = 14.5$ GeV.

5.3 Energy Loss Corrections

Particles passing through the detector material lose energy as they travel. The track momentum is reconstructed by fitting a helical path to the track points left in the detector. For this procedure all particles are assumed to be pions and the reconstructed momentum is corrected by the amount of energy loss for a pion. Fitting the track points to an ideal helical track tends to underestimate the momentum due to these energy loss effects.

For kaons and protons (or anything that is not a pion) the amount of energy loss can be determined from simulated tracks run through GEANT. The average energy loss in each p_T bin is fit to:

$$E_{Loss}(p_T) = a + b p_T^{-c} \quad (13)$$

This form does a good job of capturing the energy loss observed from the simulated and reconstructed tracks. Using this parameterization also helps smooth the fluctuations due to low statistics and noise. The energy loss corrections are applied to the raw p_T before p_T bins are determined and before all other corrections are applied.

Table 7: Energy Loss Fit Results

Species	a	b	c
π^+	-0.000550	-0.000433	-7.12
π^-	-0.000537	-0.000609	-5.58
K^+	0.000502	-0.00109	1.78
K^-	0.000247	-0.00105	1.76
P	0.00754	-0.00909	1.22
\bar{P}	0.00830	-0.00974	1.19

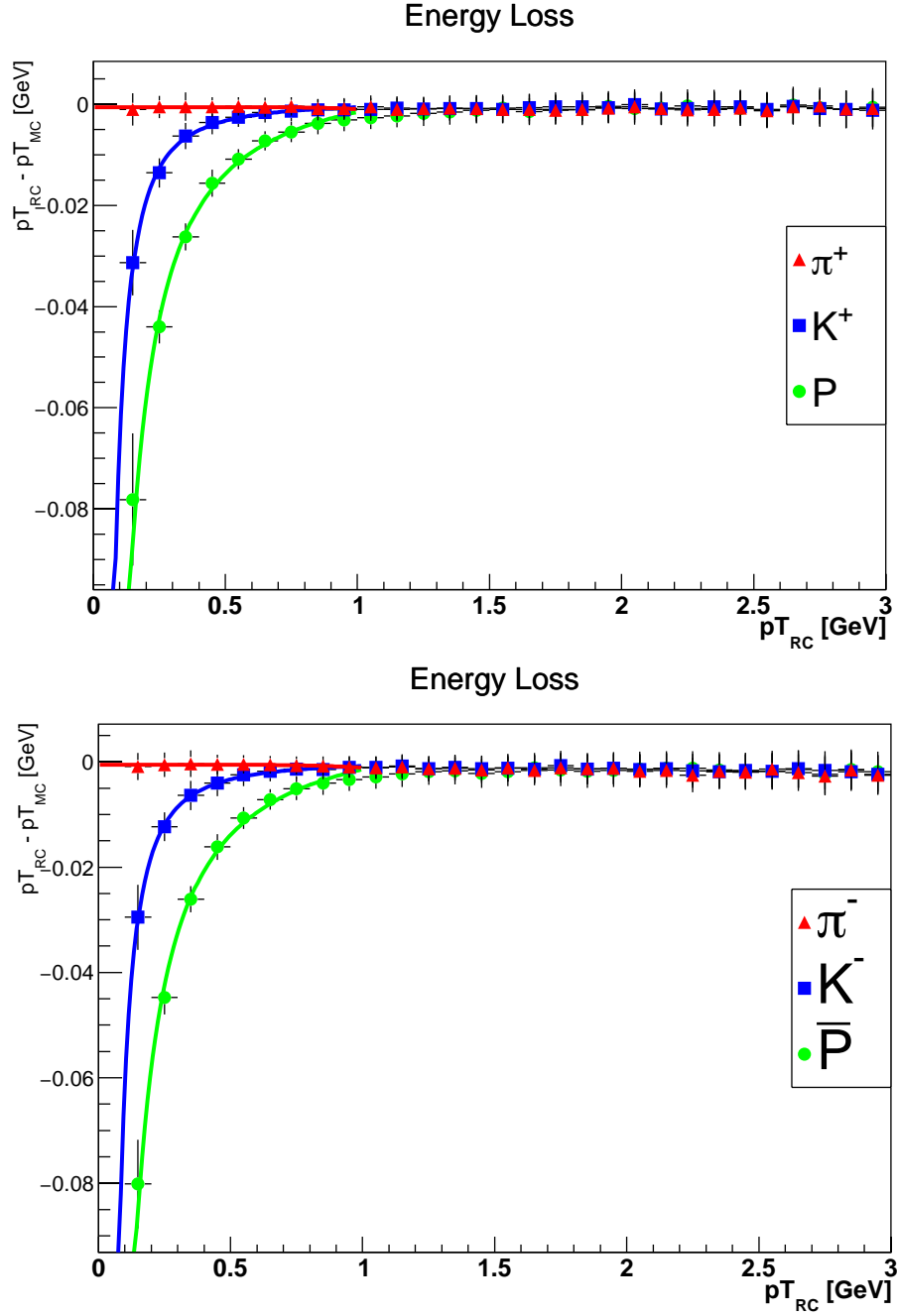


Figure 50: Energy loss results for positive (top) and negative (bottom) particles. These plots show the average energy loss across all centralities.

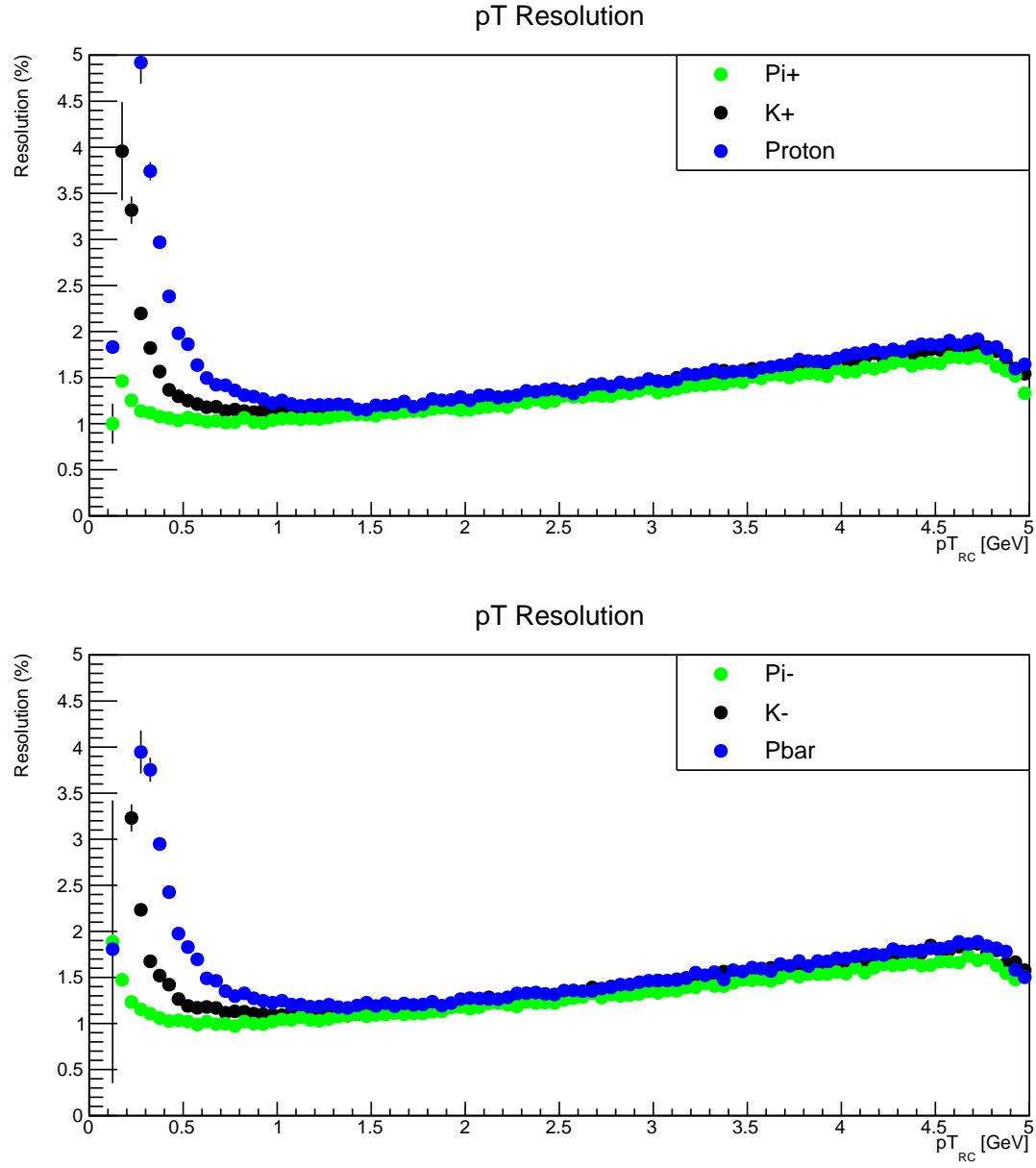


Figure 51: Momentum resolution calculated in the energy loss procedure. The momentum resolution effects are partially corrected for in the simultaneous re-centering procedure discussed in Section 5.1.1. A systematic uncertainty is also assigned to address the effects of finite momentum resolution.

5.4 Feed Down Corrections

For the purposes of this analysis, we are interested in the particles created in the initial interaction between the two gold nuclei. However, additional particles are created from subsequent decays and interactions with detector material. We wish to quantify and remove these contributions from the overall spectra as a function of p_T . For this task, we use the UrQMD simulation framework to produce 100K events from Au+Au Collisions at $\sqrt{s_{NN}} = 14.5$ GeV. Next the events are forward modeled through the STAR detector geometry using STARSIM, a GEANT3 based simulation of the STAR geometry. Finally, the detector responses generated from STARSIM are fed through the event and track reconstruction system. This results in standard STAR MuDsts and MiniMC files that can be easily analyzed with common STAR software.

Using the previously discussed method allows the feed down contributions of each species to be quantified as a function of p_T for each particle species, charge and centrality bin. It was found that $K^{+/-}$ contributions from Feed down are less than .001% for all centralities and are therefore not corrected for. An additional systematic is given to cover any uncertainty in the Kaon feed down.

The simulated data from UrQMD provides information about the parent of each particle. This information can be used to separate particles produced in the primary interaction from those produced from secondary decays or interactions with material. These feeddown contributions for $\pi^{+/-}$, p , and \bar{p} are parameterized by fitting the fraction of particles that do not originate from the primary vertex with respect to all particles of a given species. These fractions are fit for each centrality as a function of p_T using the functional forms listed in Table 8.

Table 8: Feeddown parameterizations for pions and protons

Particle Species	Parameterization of Background Fraction
π^+	$p_0 p_T^{- p_1 } + p_2 e^{-p_3 p_T}$
π^-	$p_0 e^{-p_1 p_T} + p_2 e^{-p_3 p_T}$
p	$p_0 e^{-p_1 p_T} + p_2 e^{-p_3 p_T^2}$
\bar{p}	$(p_0 + p_1 p_T^{p_2})^{-1}$

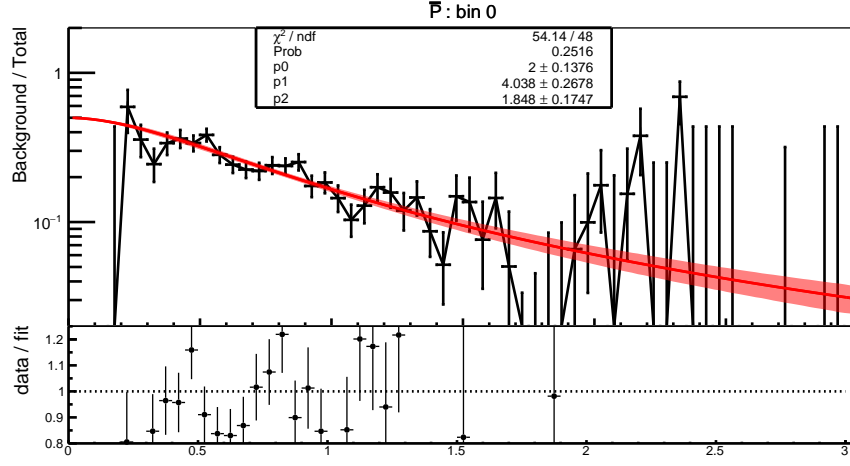


Figure 56: Fit to the fraction of background from feeddown in anti-protons as a function of p_T in 0-5% central events.

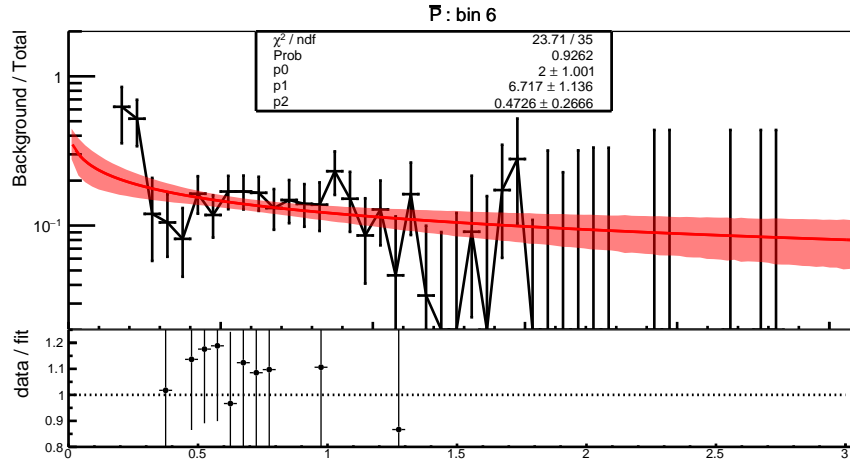
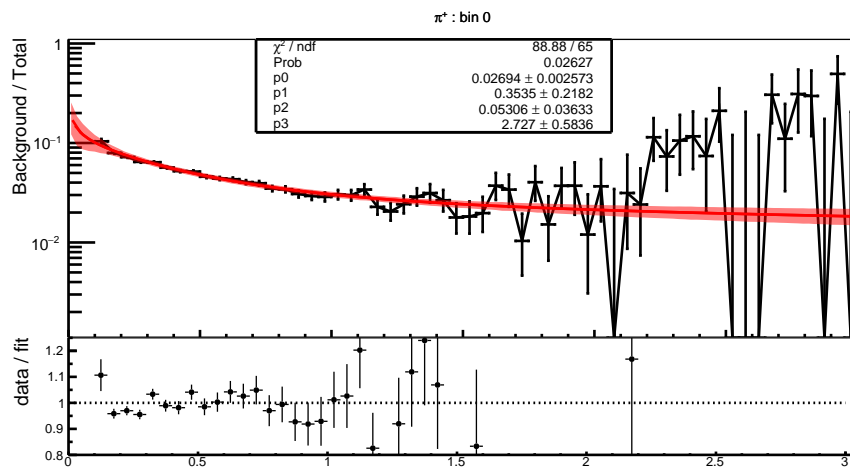
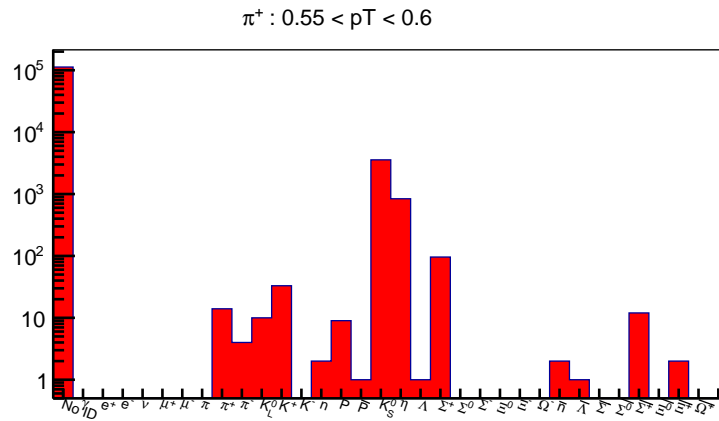
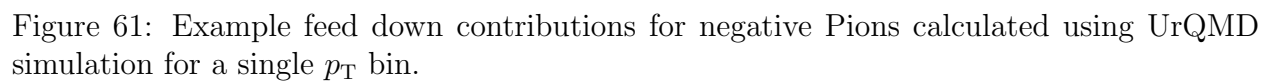


Figure 57: Fit to the fraction of background from feeddown in anti-protons as a function of p_T in 60-80% central events.





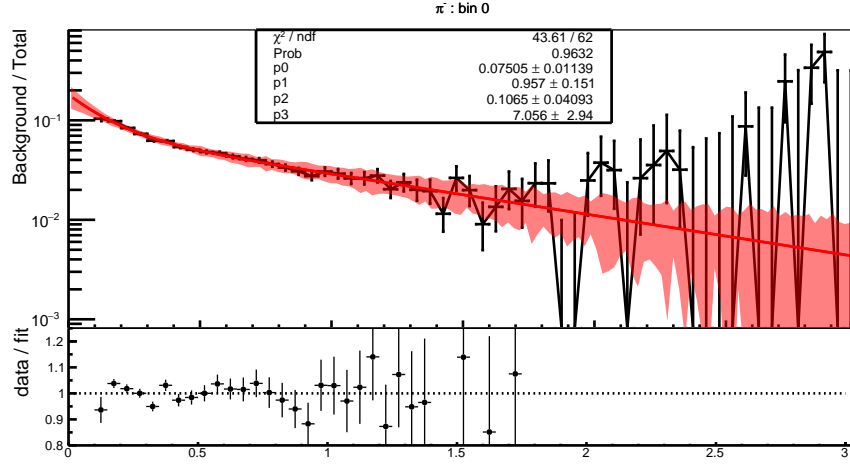


Figure 62: Fit to the fraction of background from feeddown in negative pions as a function of p_T in 0-5% central events.

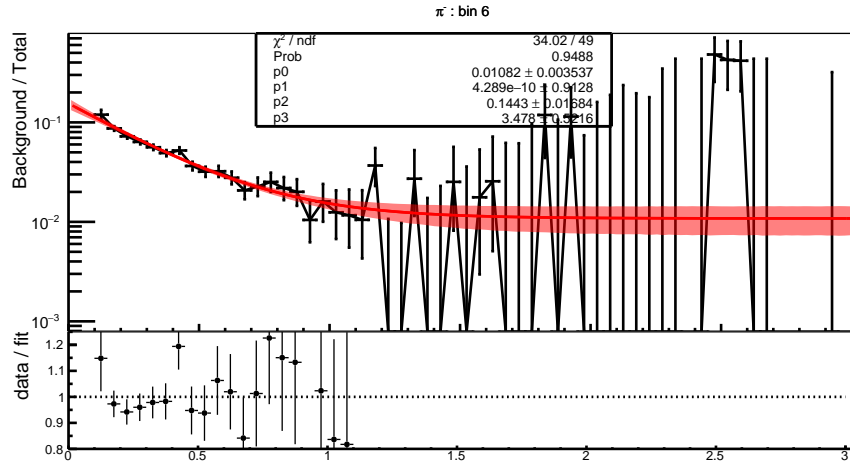


Figure 63: Fit to the fraction of background from feeddown in negative pions as a function of p_T in 60-80% central events.

6 Summary

In summary, the disappearance of high- p_T suppression in charged hadron R_{CP} as collision energy is reduced is observed for charged hadrons and identified particles. The lack of suppression at lower energies does not directly lead to the conclusion that a QGP is not being formed because we are actually interested in the suppression relative to a Cronin-like enhancement. Mesons and baryons are observed to have different trends with the R_{CP} of high- p_T baryons being enhanced at every energy in the RHIC BES. This points toward pion R_{CP} as a cleaner observable for medium induced jet-quenching than charged hadrons. Finally, using a new method developed in this paper we have measured relative suppression in 0-5% relative to 10-20% centralities all the way down to $\sqrt{s_{NN}} = 14.5$ GeV.

References

- [1] I. Arsene et al. Quark gluon plasma and color glass condensate at RHIC? The Perspective from the BRAHMS experiment. *Nucl.Phys.*, A757:1–27, 2005.
- [2] B.B. Back et al. The PHOBOS perspective on discoveries at RHIC. *Nucl.Phys.*, A757:28–101, 2005.
- [3] John Adams et al. Experimental and theoretical challenges in the search for the quark gluon plasma: The STAR Collaboration’s critical assessment of the evidence from RHIC collisions. *Nucl.Phys.*, A757:102–183, 2005.
- [4] K. Adcox et al. Formation of dense partonic matter in relativistic nucleus-nucleus collisions at RHIC: Experimental evaluation by the PHENIX collaboration. *Nucl.Phys.*, A757:184–283, 2005.
- [5] Michael J. Fromerth, Inga Kuznetsova, Lance Labun, Jean Letessier, and Jan Rafelski. From Quark-Gluon Universe to Neutrino Decoupling: 200;T;2MeV. *Acta Phys.Polon.*, B43(12):2261–2284, 2012.
- [6] Miklos Gyulassy and Larry McLerran. New forms of QCD matter discovered at RHIC. *Nucl. Phys.*, A750:30–63, 2005.
- [7] Y. Aoki, G. Endrodi, Z. Fodor, S. D. Katz, and K. K. Szabo. The Order of the quantum chromodynamics transition predicted by the standard model of particle physics. *Nature*, 443:675–678, 2006.
- [8] Szabolcs Borsanyi, Zoltan Fodor, Christian Hoelbling, et al. Is there still any T_c mystery in lattice QCD? Results with physical masses in the continuum limit III. *JHEP*, 09:073, 2010.
- [9] J. Cleymans, H. Oeschler, K. Redlich, and S. Wheaton. Comparison of chemical freeze-out criteria in heavy-ion collisions. *Phys. Rev.*, C73:034905, 2006.
- [10] Shinji Ejiri. Canonical partition function and finite density phase transition in lattice QCD. *Phys. Rev.*, D78:074507, 2008.
- [11] E. S. Bowman and J. I. Kapusta. Critical points in the linear σ model with quarks. *Phys. Rev. C*, 79:015202, Jan 2009.
- [12] M.M. Aggarwal et al. An Experimental Exploration of the QCD Phase Diagram: The Search for the Critical Point and the Onset of De-confinement. 2010.
- [13] J.D. Bjorken. Energy Loss of Energetic Partons in Quark - Gluon Plasma: Possible Extinction of High p(t) Jets in Hadron - Hadron Collisions. *FERMILAB-PUB-82-059-THY*, 1982.

- [14] Xin-Nian Wang and Miklos Gyulassy. Gluon shadowing and jet quenching in A + A collisions at $s^{*}(1/2) = 200$ -GeV. *Phys.Rev.Lett.*, 68:1480–1483, 1992.
- [15] J.D. Jackson. *Classical electrodynamics*. Wiley, 1975.
- [16] Michael L. Miller, Klaus Reygers, Stephen J. Sanders, and Peter Steinberg. Glauber modeling in high energy nuclear collisions. *Ann.Rev.Nucl.Part.Sci.*, 57:205–243, 2007.
- [17] J. J. Aubert et al. The ratio of the nucleon structure functions $F2_n$ for iron and deuterium. *Phys. Lett.*, B123:275, 1983.
- [18] I. Helenius, K.J. Eskola, H. Honkanen, and C.A. Salgado. EPS09s and EKS98s: Impact parameter dependent nPDF sets. *Nucl.Phys.*, A904-905:999c–1002c, 2013.
- [19] Serguei Chatrchyan et al. Study of high-pT charged particle suppression in PbPb compared to pp collisions at $\sqrt{s_{NN}} = 2.76$ TeV. *Eur.Phys.J.*, C72:1945, 2012.
- [20] Betty Bezverkhny Abelev et al. Neutral pion production at midrapidity in pp and Pb-Pb collisions at $\sqrt{s_{NN}} = 2.76$ TeV. 2014.
- [21] J.W. Cronin, Henry J. Frisch, M.J. Shochet, et al. Production of Hadrons with Large Transverse Momentum at 200-GeV, 300-GeV, and 400-GeV. *Phys.Rev.*, D11:3105, 1975.
- [22] D. Antreasyan, J.W. Cronin, Henry J. Frisch, et al. Production of Hadrons at Large Transverse Momentum in 200-GeV, 300-GeV and 400-GeV p p and p n Collisions. *Phys.Rev.*, D19:764–778, 1979.
- [23] P.B. Straub, D.E. Jaffe, Henry D. Glass, et al. Nuclear dependence of high x(t) hadron and high tau hadron pair production in p A interactions at $s^{*}(1/2) = 38.8$ -GeV. *Phys.Rev.Lett.*, 68:452–455, 1992.
- [24] Ivan Vitev. Initial state parton broadening and energy loss probed in d+au at {RHIC}. *Physics Letters B*, 562(12):36 – 44, 2003.
- [25] A Accardi and M Gyulassy. Cronin effect vs. geometrical shadowing in d+au collisions at {RHIC}. *Physics Letters B*, 586(34):244 – 253, 2004.
- [26] V. Greco, C.M. Ko, and P. Levai. Parton coalescence at RHIC. *Phys.Rev.*, C68:034904, 2003.
- [27] A. Adare et al. Neutral pion production with respect to centrality and reaction plane in Au+Au collisions at $\sqrt{s_{NN}}=200$ GeV. *Phys.Rev.*, C87(3):034911, 2013.
- [28] K.H. Ackermann et al. STAR detector overview. *Nucl.Instrum.Meth.*, A499:624–632, 2003.
- [29] M. Anderson, J. Berkovitz, W. Betts, et al. The Star time projection chamber: A Unique tool for studying high multiplicity events at RHIC. *Nucl.Instrum.Meth.*, A499:659–678, 2003.

- 489 [30] W.J. Llope. Multigap RPCs in the STAR experiment at RHIC. *Nucl.Instrum.Meth.*,
490 A661:S110–S113, 2012.
- 491 [31] M. M. Aggarwal et al. Scaling properties at freeze-out in relativistic heavy ion collisions.
492 *Phys. Rev.*, C83:034910, 2011.
- 493 [32] M. Bleicher, E. Zabrodin, C. Spieles, et al. Relativistic hadron hadron collisions in the
494 ultrarelativistic quantum molecular dynamics model. *J.Phys.*, G25:1859–1896, 1999.
- 495 [33] J. Allison, K. Amako, J. Apostolakis, et al. Geant4 developments and applications.
496 *Nuclear Science, IEEE Transactions on*, 53(1):270–278, Feb 2006.
- 497 [34] S. Agostinelli, J. Allison, K. Amako, et al. Geant4a simulation toolkit. *Nuclear In-*
498 *struments and Methods in Physics Research Section A: Accelerators, Spectrometers,*
499 *Detectors and Associated Equipment*, 506(3):250 – 303, 2003.
- 500 [35] Rene Brun, Federico Carminati, and Simone Giani. GEANT Detector Description and
501 Simulation Tool. 1994.

502

A

503

Bad Run Numbers

Table 9: Run #s Marked as Bad in Run10 Au+Au 7.7 GeV

Run #	Run #	Run #	Run #	Run #	Run #	Run #	Run #
11125004	11125021	11124018	11123015	11124035	11119003	11124052	11120023
11119020	11124069	11123066	11120040	11123083	11122080	11119054	11116028
11115025	11123100	11119071	11115042	11119088	11115093	11134032	11125005
11124002	11125022	11124019	11123016	11119004	11124053	11123050	11125073
11122047	11121044	11123067	11122064	11123084	11122081	11119055	11115026
11123101	11114074	11143026	11129018	11134067	11125006	11124003	11125023
11123017	11124037	11124054	11123051	11122048	11119022	11120042	11122065
11123085	11117033	11122082	11123102	11122099	11115044	11119090	11116064
11115078	11125007	11124004	11123001	11125024	11124055	11122049	11123069
11122066	11116014	11115011	11123086	11117034	11122083	11119057	11115028
11123103	11115062	11117085	11143028	11137044	11125008	11124005	11121013
11119007	11123053	11119024	11125093	11122067	11122084	11123104	11122101
11115080	11114111	11136008	11133016	11132013	11134053	11124006	11123003
11121014	11123054	11120028	11122051	11123071	11120045	11122068	11118039
11123088	11120062	11117036	11122085	11115064	11117104	11114095	11138049
11129022	11124007	11123004	11123021	11124041	11124058	11123055	11122052
11119026	11121049	11123072	11117020	11122069	11121066	11123089	11122086
11123106	11119077	11116068	11117088	11135058	11124008	11123005	11123022
11123039	11136163	11119010	11118007	11123056	11120030	11122053	11118024
11125096	11122070	11121067	11123090	11122087	11115032	11117055	11117089
11125012	11124009	11123023	11123040	11122037	11124060	11118008	11123057
11122054	11125097	11122071	11123091	11117039	11122088	11119062	11116070
11117090	11115084	11114098	11143016	11146059	11126016	11125013	11124010
11123007	11128056	11123024	11122038	11124061	11123058	11122055	11119029
11123075	11120049	11118043	11123092	11120066	11122089	11120083	11116071
11136013	11125014	11124011	11130080	11123025	11121019	11122039	11124062
11123059	11117007	11119030	11123076	11120050	11122073	11118044	11123093
11122090	11116072	11115069	11114100	11136014	11141063	11142117	11134076
11132070	11125015	11124012	11123026	11124046	11122040	11124063	11123060
11122057	11116005	11123077	11115019	11123094	11115036	11119082	11117076
11116073	11145008	11133006	11129028	11125016	11127039	11124013	11123010
11123027	11124047	11123044	11124064	11122058	11123078	11122075	11115020
11123095	11120069	11117043	11122092	11119100	11114085	11144040	11136067
11138124	11125017	11124014	11123028	11121022	11120019	11124065	11123062
11122059	11123079	11117044	11114086	11125001	11124015	11123012	11123029
11124049	11121023	11123046	11120020	11124066	11122060	11115005	11123080
11122077	11123097	11117045	11122094	11119068	11117062	11145028	11135032
11125002	11126022	11125019	11124016	11124050	11124067	11118015	11123064
11122061	11121058	11123081	11122078	11123098	11117046	11122095	11117063
11122112	11114088	11128012	11125003	11126023	11125020	11124017	11123014
11124051	11119019	11118016	11123065	11120039	11122062	11123082	11117030
11122079	11116027	11123099	11122096 ⁶³	11122113	11119087	11116061	11117098

Table 10: Run #s Marked as Bad in Run14 Au+Au14.5 GeV

Run #	Run #	Run #	Run #
15053027	15054054	15059057	15068013
15053028	15055018	15059058	15068014
15053029	15055137	15061001	15068016
15053034	15056117	15061009	15068018
15053035	15057055	15062006	15069036
15053052	15057059	15062069	15070008
15053054	15058006	15065012	15070009
15053055	15058011	15065014	15070010
15054053	15058021	15066070	